Astrocytic modulation of population encoding in mouse visual cortex via GABA transporter 3 revealed by multiplexed CRISPR/Cas9 gene editing

Authors: Jiho Park[1,2,7], Grayson O. Sipe[3,7], Xin Tang[4,5], Prachi Ojha[2], Giselle Fernandes[2], Yi Ning Leow[1,2], Caroline Zhang[1], Yuma Osako[2], Arundhati Natesan[2], Gabrielle T. Drummond[1,2], Rudolf Jaenisch[6], Mriganka Sur[1,2]*

Affiliations:

[1]Department of Brain and Cognitive Sciences, Massachusetts Institute of Technology, Cambridge, MA, 01239, USA

[2]Picower Institute for Learning and Memory, Massachusetts Institute of Technology, Cambridge, MA, 02139, USA

[3]Department of Biology, Eberly College of Science and Huck Institutes of the Life Sciences, Pennsylvania State University, University Park, PA 16802, USA

[4]F.M. Kirby Neurobiology Center, Boston Children's Hospital, Harvard Medical School, Boston, MA, 02115, USA

[5]Department of Neurosurgery, Boston Children's Hospital, Boston, MA, 02115, USA

[6]Whitehead Institute for Biomedical Research, Cambridge, MA, 02142, USA

[7]These authors contributed equally

*Corresponding author. Email: msur@mit.edu

Summary

Astrocytes, which are increasingly recognized as pivotal constituents of brain circuits governing a wide range of functions, express GABA transporter 3 (Gat3), an astrocyte-specific GABA transporter responsible for maintenance of extra-synaptic GABA levels. Here, we examined the functional role of Gat3 in astrocyte-mediated modulation of neuronal activity and information encoding. First, we developed a multiplexed CRISPR construct applicable for effective genetic ablation of Gat3 in the visual cortex of adult mice. Using *in vivo* two-photon calcium imaging of visual cortex neurons in Gat3 knockout mice, we observed changes in spontaneous and visually driven single neuronal response properties such as response magnitudes and trial-to-trial variability. Gat3 knockout exerted a pronounced influence on population-level neuronal activity, altering the response dynamics of neuronal populations and impairing their ability to accurately represent stimulus information. These findings demonstrate that Gat3 in astrocytes profoundly shapes the sensory information encoding capacity of neurons and networks within the visual cortex.

Introduction

Astrocytes, once thought to provide only passive support to neurons, are now recognized as active modulators of neuronal activity and behavior. Many recent studies have demonstrated that astrocytes significantly influence neuronal activity via diverse mechanisms that include regulation of the release and clearance of neurotransmitters and other neuroactive molecules at synaptic and extra-synaptic sites[1–6]. A notable mechanism through which astrocytes could impact cortical dynamics is by modulating inhibitory transmission, as astrocytes express a rich repertoire of GABA-related proteins that enable them to synthesize, release, and clear GABA[7,8]. They are often found spatially co-localized with GABAergic synapses, placing them in a position to regulate inhibitory synapses and influence local synaptic transmission, and thus network dynamics and behavior[9,10]. However, the specific effects of astrocytic modulation of inhibitory signaling on functional neuronal circuits remain unknown.

Astrocytes can shape inhibitory signaling via two major GABA transporters in the adult central nervous system: Gat1 (*SLC6A1*) and Gat3 (*SLC6A11*). While Gat1 is expressed by both neurons and astrocytes, it is localized to synaptic clefts and seems to be mostly neuronal[11–13]. Its localization makes it ideal for rapid removal of synaptic GABA, thereby facilitating efficient signal transmission between neurons[14]. On the other hand, Gat3 is exclusively expressed in astrocytic processes and is speculated to regulate tonic, rather than phasic, inhibition in neurons via reuptake of GABA from extra-synaptic space[13,15]. Tonic inhibition mediated by extra-synaptic GABA receptors is important for modulating the gain and maintaining the tone of neuronal activity via regulating neuronal excitability[16–18]. Our current understanding of Gat3 function is limited to pharmacological studies conducted in subcortical structures including the hippocampus and striatum which have mostly been done *ex vivo*. The findings from such studies have shown that

Gat3 can significantly influence single neuron properties, observed as changes in extracellular GABA levels and inhibitory postsynaptic currents (IPSCs) in cell-type-specific and state-dependent manner[12,19–21].

Gat3 has been implicated in several neurological conditions: reduction of Gat3 in the thalamus due to reactive astrogliosis leads to neuronal hyperexcitability and an increased risk of seizures[22]; increased Gat3 activity in the striatum causes excessive self-grooming behavior in mice[23]; and Gat3 reduction in globus pallidus impairs motor coordination[24,25]. Despite these findings, our understanding of the role of Gat3 in the cerebral cortex remains limited and even obscured by somewhat contradictory findings. For example, two studies have yielded contrasting results, with one study showing that pharmacological manipulation of Gat3 increases interneuron excitability[26] but another showing that it has no effect on synaptic transmission or cell excitability[27]. This suggests that Gat3 function may vary by cell type, brain region, and context, necessitating precise and controlled manipulation techniques for further investigation.

Our understanding of Gat3's impact on functional circuits *in vivo* has been hampered by a lack of experimental tools to achieve precise manipulation of Gat3. Pharmacological agents often have off-target effects and, particularly when administered systemically, can introduce confounding variables due to macroscale circuit changes and adaptations. While transgenic Gat3 knockout (KO) mice are not commercially available, this approach can also lead to developmental complications that obscure the acute impact of Gat3 on network function[28]. To address these limitations, we developed a multiplexed CRISPR construct that allows *in vivo* delivery of multiple CRISPR knockout sgRNAs and can be used with commercially available mouse lines with conditional Cas9 overexpression for rapid and efficient cell-type-specific knockout of genes in adult animals. This tool enabled us to perform the first *in vivo* investigation of astrocyte Gat3 function at both single neuron and population levels in the cortex. We hypothesized that astrocytes organize neuronal activity in the cortex by regulating tonic inhibition via Gat3 to optimize information encoding at the level of single neuronal responses and population dynamics. To test this hypothesis, we used *in vivo* two-photon imaging to capture neuronal activity in the mouse visual cortex, assessing changes at individual and collective neuronal responses induced by astrocyte Gat3 ablation.

Results

Gat3 expression spans all cortical layers

Previous studies have shown that Gat3 is expressed across the brain: it is found in all cortical layers, as well as in subcortical structures such as the thalamus and the hypothalamus[29]. We first examined the expression of Gat3 in primary visual cortex (V1). Immunohistochemical staining of adult mouse V1 revealed that Gat3 expression was found throughout the visual cortex. The overlay of GFAP promoter-driven tdTomato fluorescence and Gat3 antibody staining showed co-localization of Gat3 expression with astrocytic processes (Figures 1A and 1B). Consistent with

earlier findings, we observed expression across all cortical layers, with enriched Gat3 expression especially in layers 2/3 to 5[11,14,15] (Figure 1C).

Gat3 function can be studied *in vivo* with a single multiplexed CRISPR construct

We first used an antagonist selective for Gat3, SNAP-5114, to investigate the role of Gat3 in responses of V1 neurons *in vivo* (Figure S1). Previous work has demonstrated the effects of SNAP-5114 using *ex vivo* slice electrophysiology[12,21,23] in brain regions such as the thalamus or striatum, where Gat3 expression is significantly different than that in the cortex[15]. Our analysis of neuronal activity after systemic administration of SNAP-5114 showed subtle changes with high variability in responses in both control and experimental conditions (Figure S2). The major result from this study was a significant reduction in the maximal response of V1 neurons after SNAP-5114 administration (Figure S2B), with no change in the orientation selectivity index (OSI) of neurons (Figure S2D). Combined with inconclusive evidence from previous studies and considering the limitations of the use of pharmacological interventions for investigation of specific protein function, our findings highlighted the need for a more precise technique to effectively manipulate Gat3 to study its function *in vivo*.

The lack of commercially available transgenic mice for conditional Gat3 KO prompted us to develop an astrocyte-specific gene editing tool easily applicable to *in vivo* experiments. Therefore, we developed a multiplexed CRISPR/Cas9-based tool, Multiple sgRNA Csy4-mediated Universal Targeting System (MRCUTS), to selectively knock out one or more astrocytic genes with spatial and temporal selectivity. We opted to use a single AAV construct containing multiple CRISPR guide-RNA (gRNA) sequences delivered into transgenic mice expressing the Cas9 enzyme. In order to package multiple gRNAs in a single AAV vector, we separated 6 different single gRNAs targeting *Slc6a11* (the gene encoding Gat3) with 'cut sites' specific to the Csy4 enzyme (Figure 2A). Csy4-based RNA processing has been previously used for multiplexed gRNA delivery, though to our knowledge not to manipulate astrocyte genes[30,31]. The six gRNAs were specific to exons 1, 2, and 5 (two gRNAs each) of *Slc6a11*. The knockout (KO) efficacy of the Gat3-MRCUTS construct was validated *in vitro* via western blot (Figure 2B). We performed DNA sequencing from adult mouse brain tissue samples 4 weeks after the virus injection (C57BL/6J mice for control and CAG-Cas9-EGFP transgenic mice for Gat3 KO) to evaluate the efficacy of Gat3 KO *in vivo* (Figure 2C). In Gat3 KO samples, the gRNA-targeted areas showed a significantly higher level of genetic variants, especially deletions, in the Gat3 genomic region compared to control mice, which received the same sgRNA construct but did not express the Cas9 gene editing effector (Figure 2C). These experiments validated the efficacy of our CRISPR construct in knocking out Gat3 from astrocytes both *in vitro* and *in vivo*. Furthermore, *post hoc* immunohistochemistry of brain slices after two-photon imaging *in vivo* indicated that there was a significant reduction of Gat3 expression at the sites of injection in the Gat3 KO mice (Figures 2D-F). While most of the control brain slices showed negligible Gat3 expression differences between the hemispheres (Figures 2E, 2F, and animal 2 in Figure S3A), a few showed noticeable Gat3 reduction at the injection site (the maximal effect is shown in animal 1, Figure S3A). This

suggested that inflammatory responses to AAV injection may lead to changes in Gat3 expression, albeit with high variability between animals[22]. Nonetheless, the extent of Gat3 KO in Cas9+ mice was significantly greater than that in wild-type mice (Figure 2E, 2F, and S3B). These observations show that our multiplexed CRISPR construct reduced Gat3 expression with high efficacy. Importantly, our construct resulted in precise co-localization with neuronal jRGECO1a expression (Figure 2E), which validated our approach for studying Gat3 function *in vivo*.

To investigate the physiological effects of Gat3 reduction in the brains of Gat3 KO mice, we performed whole-cell patch clamp recordings of spontaneous inhibitory post-synaptic currents (sIPSCs) in L2/3 pyramidal neurons (Figure 2G). In the Gat3 KO slices, pyramidal neurons had an increased sIPSC frequency but not amplitude (Figures 2H-K). These changes may arise from: (1) increased ambient GABA, which may diffuse into the synaptic cleft and affect sIPSC events; (2) desensitization of presynaptic $GABA_B$ receptors that normally have inhibitory effects on GABA release, which may increase spontaneous GABA release; (3) decreased disinhibition, which may increase the inhibitory output onto excitatory neurons[26]. Regardless of mechanism, these results confirm that our multiplexed CRISPR construct reliably knocks out Gat3 in the mouse brain, leading to changes at DNA, protein, and electrophysiological levels.

Region-specific knockout of Gat3 in the visual cortex alters response properties of individual neurons

As Gat3 KO can have network-level impact on neural representations, we sought to examine its effects in V1 *in vivo* with two-photon imaging. We co-injected Gat3-MRCUTS with a construct encoding a red-shifted calcium indicator (jRGECO1a) selectively in neurons in V1 in either wild-type mice or transgenic mice with constitutive Cas9-EGFP expression for control and Gat3 KO, respectively (Figure 3A). Visual encoding in the cortex requires an intricate coordination of excitation and inhibition that changes with the release of neuromodulators across brain states[32,33]. Therefore, we also tracked locomotion and pupil dynamics to determine how Gat3 manipulation affects visual processing across dynamic brain states (Figure 3B). Three sets of isoluminant visual stimuli were presented: static gray, drifting gratings, and natural movies.

We first determined whether Gat3 KO influenced spontaneous activity of neurons. A comparison of average Ca^{2+} traces of neurons in response to a static gray screen from each group showed that neurons in the Gat3 KO animals have reduced frequency of Ca^{2+} peaks (Figure 3C). There was a decrease in the average firing rate from deconvolved calcium activity of all neurons and an overall shift in firing rate distribution in Gat3 KO animals (Figures 3D, 3E, S4A, and S4B). This is consistent with the expectation that reduced Gat3 expression would result in increased tonic GABA concentrations that consequently decrease neuronal excitability. We then examined if Gat3 KO affects spontaneous neuronal pairwise correlations, which reflect neuronal synchrony and functional connectivity. We found no significant difference in pairwise correlation coefficients between neurons in control compared to Gat3 KO animals (Figures 3F and S4C). Together, these findings suggest that Gat3 KO decreases overall neuronal activity without disrupting the underlying functional connectivity.

To investigate the impact of Gat3 KO on visual encoding, we examined if visually evoked activity of visually responsive neurons were altered in Gat3 KO animals. Consistent with our observation of spontaneous activity, neuronal responses to drifting gratings were attenuated in the Gat3 KO animals (Figure 4A). To quantify changes in response amplitude, we calculated each neuron's maximum response magnitude to its preferred orientation and found that the average response magnitude was significantly lower in Gat3 KO animals compared to controls (Figures 4D and S5C). Comparison of selectivity of neurons to grating stimuli determined by orientation tuning curves and individual OSI values, along with the percentage of highly selective cells (OSI >= 0.3)[34], showed no difference between the two groups (Figures 4B, 4C, 4E, S5A and S5B). Next, we calculated reliability indices (see Methods) in order to evaluate whether Gat3 influences the trial-to-trial variability of individual neuronal responses to the same stimulus across trials[35]. We analyzed activity at the onset of visual presentation (Figures 4F and 4G) and found that Gat3 KO neurons exhibit greater trial-by-trial variability in the magnitude and timing of visual responses, as indicated by a significantly decreased reliability index compared to control neurons (Figures 4H and S6A). These findings suggest that Gat3 may regulate the amplitude and timing of neuronal visual responses without affecting their selectivity to preferred stimuli.

V1 neurons not only encode visual stimuli, but also behavioral variables such as pupil-linked arousal and locomotion[36–40]. To test whether Gat3 ablation affects neuronal encoding of visual and non-visual information, we implemented a generalized linear model (GLM)[38,39] (Figure 4I). For each neuron, we examined how well visual stimuli, pupil diameter, and locomotion predicted the actual activity of the neuron by calculating its explained variance (R^2) (see Methods). Both the distribution of R^2 values and the mean R^2 across neurons were significantly decreased in Gat3 KO animals compared to controls (Figures 4J, 4K, and S5D), suggesting a general impairment in encoding by these major predictors. To determine whether Gat3 ablation differentially affected the encoding of specific types of information across the neuronal population, we calculated the proportion of neurons that significantly encoded each individual predictor. While we observed a slight decrease in the proportion of cells encoding visual stimuli and locomotion in the Gat3 KO group, these differences did not reach statistical significance (Figure 4L). Thus, Gat3 reduction led to a more general reduction in neural encoding for both visual stimuli and behavioral state. The decrease in overall GLM performance of Gat3 KO single neurons, without a significant change in their relative ability to encode visual stimuli or behavior variables, may be related to the increased trial-to-trial variability of neuronal responses to the same stimulus (Figure 4H).

Gat3 reduction impairs information encoding of neuronal populations in visual cortex

Given the complexity of microcircuits and heterogeneity of cell types in the cortex, Gat3 manipulation may exert changes in population dynamics that are not captured by our single neuron-level analyses. To first understand how functional interactions between pairs of neurons may be influenced by Gat3, we computed two correlation metrics in response to natural movies: signal correlation, which quantifies tuning similarity between neurons, and noise correlation, which measures co-fluctuation of trial-to-trial variability (Figure S6B, see Methods)[41,42]. Signal

correlations of Gat3 KO neurons did not significantly differ from those of control neurons, suggesting that the tuning similarity of different neurons to the same set of stimuli was not affected by Gat3 ablation (Figure S6C). Similarly, noise correlations of trial-to-trial variability in neuronal responses of the Gat3 KO neurons were not significantly different from those of the control neurons, although there was a general trend of reduced correlation coefficients in the KO group (Figure S6D). These results indicated that Gat3 does not significantly influence the functional connectivity between pairs of neurons.

While the functional connectivity between pairs of neurons across the entire population may not have been significantly altered, correlations between clusters of neurons could still be influenced by the loss of Gat3. To evaluate how individual neurons may be influenced by the activity of other neurons in the population, we used a GLM to predict a target neuron's activity using neural activity from other neurons in the population during the presentation of natural movies (Figure 5A). Unlike the earlier analysis of pairwise correlations across the entire population, a GLM can identify neurons that best predict any target neuron's activity and provide greater weight to these neuronal predictors, allowing the identification of more correlated neuronal clusters. We varied the number of neurons used for training the model to assess how the encoding ability of a single neuron changes based on population sizes, ensuring a fair comparison between the control and KO neurons. In this single neuron encoding model of population dynamics, we observed that Gat3 KO neurons have a lower R^2, suggesting that activity from other neurons in the population serves as a poor predictor for neural activity (Figures 5B, 5C, S6E, and S6F). Indeed, the proportion of neurons with maximum weights greater than 0.1 was significantly lower in the Gat3 KO group (Figure 5D). This result suggested that in Gat3 KO mice, individual neurons are much more independent and less likely to have other neighboring neurons with highly correlated activity. This could reflect greater overall noise and reduced functional clusters in the population. Thus, Gat3 may exert a larger influence non-specifically at a network-level rather than at a smaller scale with high spatial specificity.

Finally, we asked whether visual information could be reliably decoded from the V1 neuronal populations using a Support Vector Machine (SVM) algorithm that classifies visual stimulus identity based on the pattern of population activity[21]. In the control group, decoding accuracy of the visual stimulus increased with the addition of neurons as features, indicating the expected result that larger populations of neurons provide a more robust representation of visual information (Figure 5E). On the other hand, the neuronal populations in the Gat3 KO group demonstrated consistently low performance, with the mean Area Under the Receiver Operator Characteristic Curve (AUROC) remaining only slightly above chance level, even with an increased number of neurons in the population. This trend was also observed in the decoding of natural movies, with significant difference in performance between the control and Gat3 KO animals (Figure 5F). In general, however, the decoding performance of natural movies by either group was better than that of drifting gratings (Figure 5F inset). This observation is likely due to the complexity of natural movies: while strong oriented edges represented by drifting gratings are well encoded by single neurons in the visual cortex, a complex set of numerous visual components

found in natural movies requires dynamic coordination in population of neurons for accurate representation[43–45]. These findings suggest that Gat3 has a role in network-wide encoding of visual stimulus information in the cortex.

Discussion

Astrocytic regulation of neuronal activity via neurotransmitter and neuromodulator systems operates at various spatial levels from individual synapses to neuronal networks[2,5,46–50]. In this study, we aimed to refine our understanding of the mechanisms by which astrocytes contribute to changes in neuronal properties by conducting the first *in vivo* investigation of Gat3 function across multiple levels of neuronal activity. We developed a CRISPR-based strategy, MRCUTS, to achieve astrocyte-specific knockout of Gat3 *in vivo*. Using MRCUTS, we selectively manipulated Gat3 expression in astrocytes to explore its role within intact neural circuits in awake mice processing visual stimuli (Figure 2). Our data revealed that Gat3 knockout altered neuronal firing rate and response reliability to external stimuli (Figures 3 and 4). These changes at the single neuron-level extended to the network-level, where Gat3 knockout impaired the information encoding capacity of neuronal populations in the visual cortex (Figure 5). These effects on cortical microcircuits, composed of diverse cell types (Figure 5G), influenced the robustness of population encoding, as evidenced by our population analyses. Taken together, our results demonstrate that astrocytes significantly influence population-level information encoding through GABA transporter-dependent mechanisms.

Previous studies support our findings by demonstrating that Gat3 modulates both excitatory and inhibitory neuronal properties, primarily via changes in tonic and phasic GABA conductance and neuronal excitability[12,13,21,25]. These studies utilized SNAP-5114 blockade of subcortical Gat3 to show a range of changes in signal transmission (sEPSCs, sIPSCs, and tonic currents). In the hippocampus, SNAP-5114 application led to increased extracellular GABA levels and IPSCs in excitatory neurons, resulting in altered synaptic transmission *ex vivo*[12]. Gat3 also modulated inhibitory signals in a cell-type-specific manner, particularly interacting with somatostatin-expressing interneurons but not parvalbumin-expressing interneurons[19,51]. In line with the earlier observations, our *ex vivo* patch clamp recording experiments showed that Gat3 reduction increases sIPSC frequency in cortical pyramidal neurons, possibly reflecting increased availability of GABA[26]. Although relatively few studies have explored SNAP-5114 beyond synaptic levels, there is evidence that astrocytes in the hippocampus can shift network excitation to tonic inhibition via the reversal of Gat3 function[20]. Additionally, a study of Gat3 in the striatum showed that its increased expression altered medium spiny neuron (MSN) activity, leading to repetitive obsessive grooming behavior[52]. While these findings are consistent with our results, most prior studies focused on subcortical regions and employed pharmacological manipulations, likely due to the challenges of astrocyte-specific genetic manipulation and the complexity of cortical dynamics. Nonetheless, they highlight that astrocytes, through Gat3 expression, can induce network-level changes that result in functional and behavioral phenotypes.

Our study revealed that localized Gat3 ablation disrupted cortical dynamics, yet attributing these effects solely to Gat3 poses several challenges. A number of studies including our own have shown that Gat3 expression is not static – it varies across development and as a result of astrocytic Ca^{2+} activity[22,51,53]. These findings raise important questions: Are the observed changes in Gat3 expression driven by activity-dependent mechanisms, homeostatic processes, or a combination of the two? Furthermore, it is unclear how genetic disruption of Gat3 might influence interactions with other key proteins. The alterations in neuronal population dynamics could result not only from the direct loss of Gat3 but also from secondary effects involving related molecules such as receptors, channels, or transporters[13,14,51]. Moreover, compensatory mechanisms—such as the potential upregulation of other GABA transporters such as Gat1—may come into effect. These factors underscore the need for further investigation to unravel the specific pathways through which Gat3 reduction affects both neuronal and broader network functions, particularly concerning upstream and downstream molecular interactions.

Our study introduces MRCUTS, the first genetic tool utilizing multiplexed CRISPR design for astrocyte manipulation, which is compatible with commercially available transgenic mouse models. In general, astrocytes have received less attention in CRISPR/Cas9 tool development compared to neurons; thus, MRCUTS provides an unique method to manipulate astrocytic genes *in vivo* simultaneously[54]. Although this study focused solely on Gat3, MRCUTS can be developed to target other genes or combinations of genes. By leveraging transgenic mice expressing Cas9 in an astrocyte-specific manner, MRCUTS offers a powerful tool for a wide range of studies examining the role of astrocytes in brain function and behavior.

Acknowledgements

We thank Taylor Johns for lab management and members of the Sur laboratory for many discussions and comments. We are grateful to Alexandria Barlowe for histology and animal colony management. This work was supported by NIH grants R01DA049005, R01MH126351, R01NS130361, and R01MH133066, MURI Grant W911NF2110328, and The Picower Institute Innovation Fund (MS); NIH Fellowship F32EY022264 (GS); Simons Foundation Autism Research Initiative Bridge to Independence award (XT); and a fellowship from The JPB Foundation (GF).

Author Contributions

Conceptualization: JP, GOS, XT, RJ, MS; Methodology: JP, GOS, XT, MS; Investigation: JP, GOS, XT, PO, GF, YNL, YO, CZ, AN, GTD; Visualization: JP, GOS, PO, GF; Funding acquisition: GOS, MS; Supervision: RJ, MS; Writing—original draft: JP; Writing—review & editing: JP, GOS, XT, YNL, MS

Declaration of Interests

The authors declare that they have no competing interests.

Materials and Methods

Animals

All experimental procedures performed in this study were approved by the Massachusetts Institute of Technology's Animal Care and Use Committee and conformed to the National Institutes of Health. Adult mice (2-4 months) were housed on a reverse 12 hr light/dark cycle with controlled temperature and ventilation. C57BL/6JA wild-type mice (Stock No 000664, Jackson Laboratory) were used as control and CAG-Cas9-EGFP (B6J.129(B6N)-Gt(ROSA)26Sortm1(CAG-cas9*,-EGFP)Fezh/J) (Stock No 026175, Jackson Laboratory) were used for constitutive expression of Cas9 protein in all cells.

Multiplex CRISPR KO construct design and AAV vector generation

CRISPR/Ca9 knockout (KO) sgRNAs were designed to target multiple obligatory protein coding exons of the mouse *Gat3* (*Slc6a11, ENSMUST00000032451.9*) gene to create insertion/deletions that abolish the gene's protein output. Two KO sgRNAs were placed adjacently within each exon to maximize gene deletion efficiency. The KO sgRNA pairs were placed on exons 1, 2, and 5 of the mouse *Gat3* gene based on mRNA transcript NM172890. For each Gat3 KO sgRNA sequence, a Csy4 enzyme target site sequence GTTCACTGCCGTATAGGCAG was added to its 5' end, and a universal CRISPR/Cas9 sgRNA backbone sequence to its 3' end. A U6::6X Gat3 KO sgRNAs cassette was designed to include a single U6 promoter, followed by six Csy4-sgRNA-backbone sequences linked in tandem. The gene fragment was synthesized by GenScript. A PX552 AAV vector backbone (Addgene #60958) was modified to insert a PGK::His tag-Csy4 expression cassette upstream of the hGH PolyA 3' UTR to replace the U6::sgRNA scaffold-hSyn::EGFP segment of the original plasmid. A number of restriction enzyme sites were placed at the 5' end of the PGK promoter for inserting the U6::6X Gat3 KO sgRNAs cassette through T4 ligation. We term the multiplex CRISPR KO construct: Multiple sgRNA Csy4-mediated Universal Targeting System (MRCUTS). AAV virus particles were packaged using the service of UNC viral core facility (AAV8.2, titer = 2E+13 vg/ml). We refer to the virus containing the multiplexed CRISPR construct targeting Gat3 as Gat3-MRCUTS in the following sections.

Mouse *Gat3* gene KO sgRNA sequences were as follows:
CGGCCACTGGAACAACAAGG, AAAACACCACGTAAGGAATC, ATAATGCCAGTTCCCAACGG, TCATCGGACTGGGCAACGTG, TTCTTCCTGGAAACGGCTCT, TGGAAGGGTACTAAGTCGAC.

Glial cell culture and Western blot

Primary astrocyte cultures were prepared from one or two-day-old neonatal C57BL/6 mice of both sexes. Brains were removed after decapitation and cortices were dissected out using a dissecting microscope. The tissues were dissociated in the enzymatic solution containing papain for 30 min at 37°C followed by mechanical trituration to obtain a single cell suspension. The collected cell

suspension was cultured in 6-well plates pre-coated with 50 µg/mL poly-D-lysine in Astrocyte medium (ScienCell) supplemented with 10% fetal bovine serum and was maintained at 37 °C in a humidified atmosphere containing 5% CO_2. The medium was changed every 3–4 days. To examine the knockout efficiency of our multiplexed CRISPR construct, astrocytes were transfected with PX458 spCas9-P2A-GFP and PX552 PGK-Csy4 6XsgRNA constructs at 10 days *in vitro* (DIV) using Lipofectamine 3000 (ThermoFisher Scientific) following manufacturer's protocol. Briefly, for transfection in a single well of a 6-well plate, 3 µg of DNA was mixed with 6 µL of Lipofectamine 3000 in 250 µL opti-MEM (ThermoFisher Scientific).

Western blot assays were performed 5 days after transfection. Cells were washed with ice-cold phosphate-buffered saline (PBS) and lysed in 1X RIPA lysis buffer (Abcam) containing protease inhibitor cocktail (Sigma). Samples were subsequently boiled in 1X NuPAGE LDS sample buffer (ThermoFisher Scientific) at 99°C for 10 min and proteins were separated on NuPAGE 4–12% Bis-Tris Gels (ThermoFisher Scientific). They were then transferred onto a PVDF membrane using the iBlot system (ThermoFisher Scientific) and blocked with 5% nonfat dry milk in 0.05% PBS-T (PBS-Tween 20) for 1 h at room temperature. Immunoblotting was then performed by incubating the membrane with either anti-GAT3 rabbit polyclonal antibody (1:1000, Synaptic Systems) or anti-β-actin mouse monoclonal antibody (1:1000, Sigma) at 4 °C overnight. Membranes were washed and incubated with the HRP-conjugated secondary antibodies (1:5000, Cell Signaling Technology) for 45 min at room temperature. Detection was carried out using the Immobilon Forte Western HRP substrate (MilliporeSigma) and images were acquired with ChemiDoc Imaging system (Bio-Rad). Data was quantified by densitometric analysis using ImageJ software and individual band intensities were normalized to β-actin.

Stereotactic surgeries

Surgeries were performed under isoflurane anesthesia (3% for induction, 1-1.5% for maintenance) while maintaining body temperature at 37.5°C. Mice were given pre-emptive slow-release buprenorphine (1 mg/kg, s.c.) and post-operative meloxicam (5 mg/kg, s.c.). Mice were head-fixed in a stereotaxic frame, scalp hair was removed, and the skin was sterilized with 70% ethanol and betadine. A portion of the scalp was removed to expose the skull.

For virus injections, we drilled 3 small craniotomies (0.5mm) per hemisphere centered around the coordinates for the visual cortex (1.5mm anterior and 2.5mm lateral to lambda) and injected a volume of 200-300nl per site at a rate of 60nl/min 200µm below the pial surface with a glass pipette and a stereotaxic injector (QSI 53311, Stoelting). The glass pipette was left in place for an additional 5 min after the injection and was slowly withdrawn to avoid virus backflow. Injections were performed in both hemispheres to maximize tissue collection. Gat3-MRCUTS and AAV1-CAG-tdTomato were co-injected to visualize the injection site for tissue collection.

For two-photon imaging experiments, a round 3 mm diameter craniotomy was performed over the left visual cortex (1.5 mm anterior and 2.5 mm lateral to lambda) and a total volume of 300-400nl of virus, split over 3 injection sites, at 60nl/min was injected 200µm below the pial surface. Gat3-MRCUTS and AAV9-hSYN-jRGECO1a were co-injected for neuronal expression

of red calcium indicator. A cranial window was prepared with 3 round coverslips (CS-5R, 1 x 5 mm diameter; CS-3R, 2 x 3 mm diameter; Warner Instruments) glued together with UV-cured adhesive (catalog #NOA 61, Norland). The cranial window was implanted over the 3 mm craniotomy and sealed with dental cement (C&B Metabond, Parkell). A headplate was fixed to the skull using the same dental cement for calcium imaging. Mice were monitored for 3 days following surgery. Mice recovered for at least 5 days before habituation and imaging experiments. After completion of experiments, mice were perfused for *post hoc* validation of Gat3 knockout efficiency.

DNA sequencing

Mice were deeply anesthetized under isoflurane and decapitated for rapid brain extraction. Cortical regions labeled with a fluorescent marker were dissected in ice-cold 0.9% saline and meninges were removed. Cortex biopsies were flash frozen and stored at −80°C. Frozen samples were later equilibrated to room temperature, cut into small pieces (≤ 25 mg) and genomic DNA was extracted using QIAamp DNA Mini Kit (Qiagen) according to the manufacturer's instructions. Genomic sites of interest were PCR amplified from purified genomic DNA using Q5 High-Fidelity DNA Polymerase (NEB) with the following primers flanking the gRNA-targeting regions of Gat3: GAT3_Locus1 Forward, GCCATGACTGCGGAGCAAGC, Reverse, ATGCACGAGAGGTGTCACCCCAC; GAT3_Locus2 Forward, TGGAATTCCAGCTGAAAGAGGGCCGT, Reverse, TCCTTTGAAACAGCCTTGGCAGCT. Amplicons were then sequenced using Primordium Premium PCR sequencing. Reads per base data was used to quantify the number of variants in the gRNA-targeting areas from the same pool of PCR amplicons within each sample and results from one gRNA-targeted region in Gat3 KO mice were represented as normalized to control.

Immunohistochemistry

Mice were transcardially perfused with 0.9% NaCl followed by 4% paraformaldehyde (PFA). Coronal sections were sectioned with a vibratome at 50μm thickness. Brain sections were incubated in a blocking solution (1% Triton X-100, 5% BSA in PBS) for 1 hr at room temperature on a shaker. Sections were incubated in the blocking solution containing primary antibody rabbit anti-GAT3 (1:500, catalog # 274 304, SySy) overnight at 4°C. Sections were washed and incubated for 4 hr in blocking solution with secondary antibody goat anti-rabbit Alexa Fluor 647 (1:1000, catalog # A32733, Invitrogen). Sections were washed in PBS and mounted on slides in DAPI containing mounting medium (VECTASHIELD, catalog #H-1500, Vector Laboratories). Images were taken using a Leica confocal microscope (TCS SP8, Leica) with a 20x/0.75 NA objective lens and LAS X Acquisition Software (Leica). The images were processed with the ImageJ software.

Slice Preparation

Adult mice (WT or CAG-Cas9-EGFP) were injected Gat3-MRCUTS targeting layer 2/3 of the visual cortex (AP: 1.5 mm; ML: 2.5 mm; DV: 0.2 mm from lambda). Mice were anesthetized using isoflurane and the brains were rapidly dissected out and transferred to oxygenated (95% O_2 / 5% CO_2), ice-cold cutting solution containing (in mM): 118 Choline chloride, 2.5 KCl, 1.2 NaH_2PO_4, 26 $NaHCO_3$, 10 Glucose, 2.5 $CaCl_2$, and 1.3 $MgCl_2$. Coronal slices (300 µm thick) containing the visual cortex were cut using a Leica VT1200S vibrating blade microtome, transferred to an oxygenated solution containing (in mM): 92 NaCl, 2.5 KCl, 1.2 NaH_2PO_4, 30 $NaHCO_3$, 20 HEPES, 25 glucose, 2 Thiourea, 5 Na-ascorbate, 3 Na-pyruvate, 5 N-acetyl-L-cysteine, 2 $CaCl_2$, and 2 $MgCl_2$ and allowed to recover for 1hr. For electrophysiological recordings, slices were transferred to a superfused recording chamber, constantly perfused with oxygenated aCSF containing (in mM): 115 NaCl, 10 glucose, 25.5 $NaHCO_3$, 1.05 NaH_2PO_4, 3.3 KCl, 2 $CaCl_2$, and 1 $MgCl_2$ and maintained at 28°C.

Whole-cell patch recordings

Whole-cell voltage-clamp recordings were performed on neurons in layer 2/3 of the visual cortex with pipettes (3-5MΩ resistance) pulled from thin-walled Borosilicate glass using a Sutter P97 Flaming/Brown micropipette puller. The pipettes were filled with an internal solution containing (in mM): 140 Cesium chloride, 10 HEPES, 0.5 EGTA, 2 $MgCl_2$, 10 phosphocreatine, 5 Mg-ATP, and 1 Na-GTP. The pH of the internal solution was adjusted to 7.3 with Cesium hydroxide and osmolarity adjusted to 295-300 mOsm. All recordings were obtained using a MultiClamp 700B (Molecular Devices) amplifier and digitized using the Digidata 1440A system (Molecular Devices). Signals were filtered at 2kHz and digitized at 10kHz. Neurons were included in the study only if the initial resting membrane potential (Vm) was $\leq$ -55 mV, access resistance (Ra) was <25MΩ and were rejected if the Ra changed by >20% of its initial value. For all recordings, neurons were held at -65 mV. Spontaneous inhibitory postsynaptic currents (sIPSCs) were isolated by blocking excitatory currents with 10µM 6-Cyano-7-nitroquinoxaline-2,3-dione disodium salt hydrate (CNQX) and 30µM D(−)-2-Amino-5-phosphonopentanoic acid (D-AP5) perfused in the bath. Continuous current traces of 5-min duration (recorded at least 5 min after achieving whole-cell configuration) were acquired and analyzed with Clampfit 10.7 (Molecular Devices). The frequency and amplitude of recorded sIPSCs were quantified.

***In vivo* two-photon imaging**

Mice were head-fixed in a behavior rig which consisted of a running wheel and a screen monitor on the right side of the wheel for presentation of visual stimuli and imaging of the left visual cortex. Imaging was performed 3-5 weeks post-virus injection and after 2-3 days of habituation. A Prairie Ultima IV two-photon microscopy system was used with a resonant-galvo scanning module (Bruker). Two-photon excitation of jRGECO1a at a 1020 nm wavelength was provided by a tunable Ti:Sapphire laser (Mai Tai eHP, SpectraPhysics) and the signal was collected by GaAsP photomultiplier tubes (Hamamatsu). Images were acquired with a 16x/0.8 NA microscope

objective (Nikon) with 2x optical zoom at 16Hz. A 512 x 256 pixel FOV was imaged for each imaging session of awake mice. The mice were presented with 3 sets of visual stimuli, a gray screen, drifting gratings, and natural movies, in 3 different imaging sessions. Movement of the mice on the wheel was tracked and recorded simultaneously. A pupil camera was placed next to the screen monitor to record pupil dynamics during the sessions.

Visual stimuli

Isoluminant visual stimuli (static gray screen, drifting bar gratings, and natural movies) were constructed by MATLAB (Mathworks) using Psychtoolbox. For spontaneous activity, a gray screen was shown for 640 s. For drifting gratings, a set of drifting gratings was presented for 2 s following a 3 s OFF period, with gratings rotated by 45° for a set of 4 orientations and 8 directions. A single trial consisted of a set of 8 grating directions, each separated by an OFF period, with 16 trials in one session. For natural movies, we used a total of 7 different black-and-white movies from the van Hateren movie data base[35,55]. Each trial started with a single OFF period for 3 s and was followed by a consecutive presentation of individual movies, each being presented for 2 s. The order of the movies remained the same and the trials were repeated 32 times in a session.

Calcium data analysis

After image acquisition, time-lapse imaging sequences were corrected for motions using a template-matching ImageJ plug-in. We used a two-photon calcium imaging analysis pipeline, Suite2P[56] to detect cells in the recorded data. Detected ROIs were manually curated to select ROIs with putative somatic activity during the imaging session. Preprocessing and basic visual response property analysis of the data (i.e. orientation selectivity and tuning curves) were carried out using custom functions written in MATLAB. We acquired the somatic fluorescence signal from the ROI by subtracting neuropil fluorescence from raw fluorescence ($F_{ROI} = F_{raw} - 0.7*F_{neuropil}$). We used *ksdensity* function to determine F_0 and calculate $\Delta F/F_0$ ($(F-F_0)/F_0$). The following analyses were done in Python: firing rates, maximum response magnitude, correlation coefficients, encoding models, and decoding analysis. The reliability indices of single neurons in response to natural movies were calculated by averaging the correlation of all pairwise combinations of trials for a single movie[35]. For computation of firing rates and pairwise correlation coefficients, we used deconvolved spikes from Suite2p as an indirect readout of spiking activity of individual neurons. For pairwise neuron-to-neuron correlation, each neuron's activity for all trials was concatenated into one vector. Pearson correlation coefficients were computed between a pair of vectors using *numpy.corrcoef* function in Python. For signal and noise correlations, only stimulus-dependent responses of individual neurons were used. For signal correlation, each neuron's responses to a set of stimuli were averaged across trials and the vector containing trial-average activity was used for Pearson correlation. For noise correlation, z-scores were computed across the trials which were then concatenated into a single vector for Pearson correlation.

Pupil dynamics

For pupil tracking we used DeepLabCut[57,58] (version 3.0.0.). Specifically, we manually labeled ~200 frames (14 frames/video) and used a mobilenet_v2_1.0-based neural network with default parameters for 50,000 training iterations to predict the location of 8 markers (xy-coordinates). Once the network was trained, it was used to place coordinates on unlabeled frames. This network was then used to analyze videos from similar experimental settings. The pupil diameter was calculated by computing the distance between pairs of xy-coordinates placed across the pupil.

Generalized Linear Model (GLM) of neuronal activity

Neuronal encoding of (1) visual stimulus, pupil diameter, and running speed and (2) population activity was modeled with a GLM for each neuron independently. A GLM with linear (identity) link function was used to compute the weights of predictors in modeling the activity of single neurons based on calcium signals. In this model, neuronal activity is described as a linear sum of visual and behavioral predictors aligned to each event. For the first encoding model, predicted neuronal activity $r_n(t)$ for a target neuron n is described as

$$r_n(t) = \sum_{c} \sum_{t_s \in S_c} \beta_{c,n}^{t_s} x_c(t - t_s) + \sum_{b} \beta_{b,n} x_b(t) + \varepsilon$$

where c represents the direction of the visual stimulus (eight directions), b represents the behavioral variables (pupil diameters and running speed), S_c represents the set of times to cover each predictor window. $\beta_{c,n}$ and $\beta_{b,n}$ represent the weights of visual stimulus and behavioral variables for neuron n. The visual stimulus predictors cover the window [0 -2] s from stimulus onset. x_c and x_b represent the visual stimulus and behavioral variable predictors, respectively. Each predictor is coded as "1" or "0" except for behavioral variables. Behavioral variable predictors are continuous behavioral event variables such as pupil diameter. ε is the model bias (intercept). The values for the behavioral variables were z-scored.

To estimate the optimal weights for each neuron without overfitting, the *lassoglm* function in MATLAB with tenfold cross-validation of the training set was used with a lasso regularization according to the value of a selected parameter λ, which represents regularization coefficients (*sklearn.linear_model.Lasso* class in Python was used for the population activity encoding model). The value of λ in the lassoglm function was set to be 10^{-3}. Model performance was assessed for the test dataset by quantifying explained variance (R^2).

To determine the proportion of neurons with a significant contribution of the variance explained by each variable, we fitted the model using full predictors (full model) and predictors in which the target predictor is set to zero within whole-time points (partial model) and calculated the explained variance ($R^2_{full}, R^2_{partial}$) for the full and partial model. We then performed a t-test between the R^2_{full}, and $R^2_{partial}$ across the 10-fold cross validation, correcting for multiple comparisons with Bonferroni-Holm correction.

Decoding analysis

We built Support Vector Machine (SVM) classifiers using *sklearn.svm.SVC* class in Python to evaluate the capacity of the V1 neuronal population to represent visual stimuli information. All population decoding was performed for each session. For the training and testing dataset, the number of trials in each condition (eight directions or 7 movies) was matched to prevent bias for training classifiers. We left a 33% subset of trials for prediction to avoid overfitting. Best estimator parameters were determined by optimization to avoid overfitting and minimize loss of validation in a grid search manner (searched range 10^{-3} to 10^{3}).

We used the mean ΔF/F response during stimulus presentation (2 seconds for gratings, 3 seconds for movies) for each individual neuron. Classifier performance on each iteration was estimated by averaging decoding accuracies across all iterations. To determine if the decoder performance was above chance, we shuffled labels for the test data, trained, and tested the decoder to assess the decoding accuracy.

For statistical assessment of the decoding accuracy between sessions, we trained and tested decoders using a subset of population of neurons (from 5 to 25 neurons, at increments of 5) by randomly choosing neurons in each iteration. The decoding performance was evaluated by calculating the Area Under the Receiver Operating Characteristic Curve (AUROC) from prediction scores of the test set. Difference in decoding accuracy between the two groups (control and Gat3 KO) was evaluated using a 2-way ANOVA to examine the effects of population size and experimental group on the decoding accuracy.

Statistics

All statistical analysis was performed using custom written scripts in MATLAB or Python. All statistical tests used are reported in the figure legends. For comparison of single neuron responses collected *in vivo*, we used linear mixed effects models (referred to as LME) to accommodate the dependency between measurements taken from the same subject[59] using *statsmodel.formula.api.mixedlm* from statsmodel[60] (version 0.14.4). Statistical comparisons employed two-tailed t-statistics. For *ex vivo* and *in vitro* experiments, we used Mann-Whitney U tests, Kolmogorov-Smirnov tests, and two-tailed unpaired t-tests as appropriate. For SVM decoding, we used a 2-way ANOVA and Mann-Whitney U test.

References

1. Santello, M., Toni, N., and Volterra, A. (2019). Astrocyte function from information processing to cognition and cognitive impairment. Nat. Neurosci. *22*, 154–166. https://doi.org/10.1038/s41593-018-0325-8.
2. Perea, G., Sur, M., and Araque, A. (2014). Neuron-glia networks: integral gear of brain function. Front. Cell. Neurosci. *8*, 378. https://doi.org/10.3389/fncel.2014.00378.
3. Volterra, A., and Meldolesi, J. (2005). Astrocytes, from brain glue to communication elements: the revolution continues. Nat. Rev. Neurosci. *6*, 626–640. https://doi.org/10.1038/nrn1722.
4. Miguel-Quesada, C., Zaforas, M., Herrera-Pérez, S., Lines, J., Fernández-López, E., Alonso-Calviño, E., Ardaya, M., Soria, F.N., Araque, A., Aguilar, J., et al. (2023). Astrocytes adjust the dynamic range of cortical network activity to control modality-specific sensory information processing. Cell Rep. *42*, 112950. https://doi.org/10.1016/j.celrep.2023.112950.
5. Khakh, B.S., and Sofroniew, M.V. (2015). Diversity of astrocyte functions and phenotypes in neural circuits. Nat. Neurosci. *18*, 942–952. https://doi.org/10.1038/nn.4043.
6. Haim, L.B., and Rowitch, D.H. (2017). Functional diversity of astrocytes in neural circuit regulation. Nat. Rev. Neurosci. *18*, 31–41. https://doi.org/10.1038/nrn.2016.159.
7. Liu, J., Feng, X., Wang, Y., Xia, X., and Zheng, J.C. (2022). Astrocytes: GABAceptive and GABAergic Cells in the Brain. Front. Cell. Neurosci. *16*, 892497. https://doi.org/10.3389/fncel.2022.892497.
8. Kwak, H., Koh, W., Kim, S., Song, K., Shin, J.-I., Lee, J.M., Lee, E.H., Bae, J.Y., Ha, G.E., Oh, J.-E., et al. (2020). Astrocytes Control Sensory Acuity via Tonic Inhibition in the Thalamus. Neuron *108*, 691-706.e10. https://doi.org/10.1016/j.neuron.2020.08.013.
9. Mederos, S., Sánchez-Puelles, C., Esparza, J., Valero, M., Ponomarenko, A., and Perea, G. (2021). GABAergic signaling to astrocytes in the prefrontal cortex sustains goal-directed behaviors. Nat. Neurosci. *24*, 82–92. https://doi.org/10.1038/s41593-020-00752-x.
10. Perea, G., Gómez, R., Mederos, S., Covelo, A., Ballesteros, J.J., Schlosser, L., Hernández-Vivanco, A., Martín-Fernández, M., Quintana, R., Rayan, A., et al. (2016). Activity-dependent switch of GABAergic inhibition into glutamatergic excitation in astrocyte-neuron networks. eLife *5*, e20362. https://doi.org/10.7554/eLife.20362.
11. Melone, M., Ciappelloni, S., and Conti, F. (2014). Plasma membrane transporters GAT-1 and GAT-3 contribute to heterogeneity of GABAergic synapses in neocortex. Front. Neuroanat. *8*. https://doi.org/10.3389/fnana.2014.00072.
12. Kersanté, F., Rowley, S.C.S., Pavlov, I., Gutièrrez-Mecinas, M., Semyanov, A., Reul, J.M.H.M., Walker, M.C., and Linthorst, A.C.E. (2013). A functional role for both -aminobutyric acid (GABA) transporter-1 and GABA transporter-3 in the modulation of extracellular GABA and GABAergic tonic conductances in the rat hippocampus. J. Physiol. *591*, 2429–2441. https://doi.org/10.1113/jphysiol.2012.246298.

13. Song, I., Volynski, K., Brenner, T., Ushkaryov, Y., Walker, M., and Semyanov, A. (2013). Different transporter systems regulate extracellular GABA from vesicular and non-vesicular sources. Front. Cell. Neurosci. *7*. https://doi.org/10.3389/fncel.2013.00023.
14. Scimemi, A. (2014). Structure, function, and plasticity of GABA transporters. Front. Cell. Neurosci. *8*. https://doi.org/10.3389/fncel.2014.00161.
15. Minelli, A., DeBiasi, S., Brecha, N.C., Zuccarello, L.V., and Conti, F. (1996). GAT-3, a high-affinity GABA plasma membrane transporter, is localized to astrocytic processes, and it is not confined to the vicinity of GABAergic synapses in the cerebral cortex. J. Neurosci. Off. J. Soc. Neurosci. *16*, 6255–6264. https://doi.org/10.1523/JNEUROSCI.16-19-06255.1996.
16. Koh, W., Kwak, H., Cheong, E., and Lee, C.J. (2023). GABA tone regulation and its cognitive functions in the brain. Nat. Rev. Neurosci., 1–17. https://doi.org/10.1038/s41583-023-00724-7.
17. Semyanov, A., Walker, M.C., Kullmann, D.M., and Silver, R.A. (2004). Tonically active GABAA receptors: modulating gain and maintaining the tone. Trends Neurosci. *27*, 262–269. https://doi.org/10.1016/j.tins.2004.03.005.
18. Lee, V., and Maguire, J. (2014). The impact of tonic GABAA receptor-mediated inhibition on neuronal excitability varies across brain region and cell type. Front. Neural Circuits *8*. https://doi.org/10.3389/fncir.2014.00003.
19. Matos, M., Bosson, A., Riebe, I., Reynell, C., Vallée, J., Laplante, I., Panatier, A., Robitaille, R., and Lacaille, J.-C. (2018). Astrocytes detect and upregulate transmission at inhibitory synapses of somatostatin interneurons onto pyramidal cells. Nat. Commun. *9*, 4254. https://doi.org/10.1038/s41467-018-06731-y.
20. Héja, L., Nyitrai, G., Kékesi, O., Dobolyi, A., Szabó, P., Fiáth, R., Ulbert, I., Pál-Szenthe, B., Palkovits, M., and Kardos, J. (2012). Astrocytes convert network excitation to tonic inhibition of neurons. BMC Biol. *10*, 26. https://doi.org/10.1186/1741-7007-10-26.
21. Boddum, K., Jensen, T.P., Magloire, V., Kristiansen, U., Rusakov, D.A., Pavlov, I., and Walker, M.C. (2016). Astrocytic GABA transporter activity modulates excitatory neurotransmission. Nat. Commun. *7*, 13572. https://doi.org/10.1038/ncomms13572.
22. Cho, F.S., Vainchtein, I.D., Voskobiynyk, Y., Morningstar, A.R., Aparicio, F., Higashikubo, B., Ciesielska, A., Broekaart, D.W.M., Anink, J.J., van Vliet, E.A., et al. (2022). Enhancing GAT-3 in thalamic astrocytes promotes resilience to brain injury in rodents. Sci. Transl. Med. *14*, eabj4310. https://doi.org/10.1126/scitranslmed.abj4310.
23. Yu, X., Taylor, A.M.W., Nagai, J., Golshani, P., Evans, C.J., Coppola, G., and Khakh, B.S. (2018). Reducing Astrocyte Calcium Signaling In Vivo Alters Striatal Microcircuits and Causes Repetitive Behavior. Neuron *99*, 1170-1187.e9. https://doi.org/10.1016/j.neuron.2018.08.015.
24. Kang, S., Hong, S.-I., Kang, S., Song, M., Yang, M.A., Essa, H., Baker, M., Lee, J., Bruce, R.A., Lee, S.W., et al. (2023). Astrocyte activities in the external globus pallidus regulate action-selection strategies in reward-seeking behaviors. Sci. Adv. *9*, eadh9239. https://doi.org/10.1126/sciadv.adh9239.

25. Chazalon, M., Paredes-Rodriguez, E., Morin, S., Martinez, A., Cristóvão-Ferreira, S., Vaz, S., Sebastiao, A., Panatier, A., Boué-Grabot, E., Miguelez, C., et al. (2018). GAT-3 Dysfunction Generates Tonic Inhibition in External Globus Pallidus Neurons in Parkinsonian Rodents. Cell Rep. *23*, 1678–1690. https://doi.org/10.1016/j.celrep.2018.04.014.
26. Kinney, G.A. (2005). GAT-3 Transporters Regulate Inhibition in the Neocortex. J. Neurophysiol. *94*, 4533–4537. https://doi.org/10.1152/jn.00420.2005.
27. Keros, S., and Hablitz, J.J. (2005). Subtype-Specific GABA Transporter Antagonists Synergistically Modulate Phasic and Tonic GABAA Conductances in Rat Neocortex. J. Neurophysiol. *94*, 2073–2085. https://doi.org/10.1152/jn.00520.2005.
28. Tang, X., Jaenisch, R., and Sur, M. (2021). The role of GABAergic signalling in neurodevelopmental disorders. Nat. Rev. Neurosci. *22*, 290–307. https://doi.org/10.1038/s41583-021-00443-x.
29. Pow, D.V., Sullivan, R.K.P., Williams, S.M., Scott, H.L., Dodd, P.R., and Finkelstein, D. (2005). Differential expression of the GABA transporters GAT-1 and GAT-3 in brains of rats, cats, monkeys and humans. Cell Tissue Res. *320*, 379–392. https://doi.org/10.1007/s00441-004-0928-0.
30. Ferreira, R., Skrekas, C., Nielsen, J., and David, F. (2018). Multiplexed CRISPR/Cas9 Genome Editing and Gene Regulation Using Csy4 in *Saccharomyces cerevisiae*. ACS Synth. Biol. *7*, 10–15. https://doi.org/10.1021/acssynbio.7b00259.
31. Kurata, M., Wolf, N.K., Lahr, W.S., Weg, M.T., Kluesner, M.G., Lee, S., Hui, K., Shiraiwa, M., Webber, B.R., and Moriarity, B.S. (2018). Highly multiplexed genome engineering using CRISPR/Cas9 gRNA arrays. PLOS ONE *13*, e0198714. https://doi.org/10.1371/journal.pone.0198714.
32. Alitto, H.J., and Dan, Y. (2010). Function of Inhibition in Visual Cortical Processing. Curr. Opin. Neurobiol. *20*, 340–346. https://doi.org/10.1016/j.conb.2010.02.012.
33. Pfeffer, C.K., Xue, M., He, M., Huang, Z.J., and Scanziani, M. (2013). Inhibition of inhibition in visual cortex: the logic of connections between molecularly distinct interneurons. Nat. Neurosci. *16*, 1068–1076. https://doi.org/10.1038/nn.3446.
34. Scholl, B., Tan, A.Y.Y., Corey, J., and Priebe, N.J. (2013). Emergence of Orientation Selectivity in the Mammalian Visual Pathway. J. Neurosci. *33*, 10616. https://doi.org/10.1523/JNEUROSCI.0404-13.2013.
35. Rikhye, R.V., and Sur, M. (2015). Spatial Correlations in Natural Scenes Modulate Response Reliability in Mouse Visual Cortex. J. Neurosci. *35*, 14661–14680. https://doi.org/10.1523/JNEUROSCI.1660-15.2015.
36. Vinck, M., Batista-Brito, R., Knoblich, U., and Cardin, J.A. (2015). Arousal and Locomotion Make Distinct Contributions to Cortical Activity Patterns and Visual Encoding. Neuron *86*, 740–754. https://doi.org/10.1016/j.neuron.2015.03.028.
37. Steinmetz, N.A., Zatka-Haas, P., Carandini, M., and Harris, K.D. (2019). Distributed coding of choice, action and engagement across the mouse brain. Nature *576*, 266–273. https://doi.org/10.1038/s41586-019-1787-x.

38. Engelhard, B., Finkelstein, J., Cox, J., Fleming, W., Jang, H.J., Ornelas, S., Koay, S.A., Thiberge, S.Y., Daw, N.D., Tank, D.W., et al. (2019). Specialized coding of sensory, motor and cognitive variables in VTA dopamine neurons. Nature *570*, 509–513. https://doi.org/10.1038/s41586-019-1261-9.
39. Osako, Y., Ohnuki, T., Tanisumi, Y., Shiotani, K., Manabe, H., Sakurai, Y., and Hirokawa, J. (2021). Contribution of non-sensory neurons in visual cortical areas to visually guided decisions in the rat. Curr. Biol. *31*, 2757-2769.e6. https://doi.org/10.1016/j.cub.2021.03.099.
40. Stringer, C., Pachitariu, M., Steinmetz, N., Reddy, C.B., Carandini, M., and Harris, K.D. (2019). Spontaneous behaviors drive multidimensional, brainwide activity. Science *364*, eaav7893. https://doi.org/10.1126/science.aav7893.
41. Cohen, M.R., and Kohn, A. (2011). Measuring and interpreting neuronal correlations. Nat. Neurosci. *14*, 811–819. https://doi.org/10.1038/nn.2842.
42. Panzeri, S., Moroni, M., Safaai, H., and Harvey, C.D. (2022). The structures and functions of correlations in neural population codes. Nat. Rev. Neurosci. *23*, 551–567. https://doi.org/10.1038/s41583-022-00606-4.
43. Graf, A.B.A., Kohn, A., Jazayeri, M., and Movshon, J.A. (2011). Decoding the activity of neuronal populations in macaque primary visual cortex. Nat. Neurosci. *14*, 239–245. https://doi.org/10.1038/nn.2733.
44. Tanabe, S. (2013). Population codes in the visual cortex. Neurosci. Res. *76*, 101–105. https://doi.org/10.1016/j.neures.2013.03.010.
45. Montijn, J.S., Meijer, G.T., Lansink, C.S., and Pennartz, C.M.A. (2016). Population-Level Neural Codes Are Robust to Single-Neuron Variability from a Multidimensional Coding Perspective. Cell Rep. *16*, 2486–2498. https://doi.org/10.1016/j.celrep.2016.07.065.
46. Delepine, C., Shih, J., Li, K., Gaudeaux, P., and Sur, M. (2023). Differential effects of astrocyte manipulations on learned motor behavior and neuronal ensembles in the motor cortex. J. Neurosci. https://doi.org/10.1523/JNEUROSCI.1982-22.2023.
47. Cahill, M.K., Collard, M., Tse, V., Reitman, M.E., Etchenique, R., Kirst, C., and Poskanzer, K.E. (2024). Network-level encoding of local neurotransmitters in cortical astrocytes. Nature, 1–8. https://doi.org/10.1038/s41586-024-07311-5.
48. Nagai, J., Yu, X., Papouin, T., Cheong, E., Freeman, M.R., Monk, K.R., Hastings, M.H., Haydon, P.G., Rowitch, D., Shaham, S., et al. (2021). Behaviorally consequential astrocytic regulation of neural circuits. Neuron *109*, 576–596. https://doi.org/10.1016/j.neuron.2020.12.008.
49. Kofuji, P., and Araque, A. (2021). Astrocytes and Behavior. Annu. Rev. Neurosci. *44*, 49–67. https://doi.org/10.1146/annurev-neuro-101920-112225.
50. Verkhratsky, A., and Nedergaard, M. (2018). Physiology of Astroglia. Physiol. Rev. *98*, 239–389. https://doi.org/10.1152/physrev.00042.2016.
51. Shigetomi, E., Tong, X., Kwan, K.Y., Corey, D.P., and Khakh, B.S. (2012). TRPA1 channels regulate astrocyte resting calcium and inhibitory synapse efficacy through GAT-3. Nat. Neurosci. *15*, 70–80. https://doi.org/10.1038/nn.3000.

52. Bojarskaite, L., Bjørnstad, D.M., Pettersen, K.H., Cunen, C., Hermansen, G.H., Åbjørsbråten, K.S., Chambers, A.R., Sprengel, R., Vervaeke, K., Tang, W., et al. (2020). Astrocytic Ca2+ signaling is reduced during sleep and is involved in the regulation of slow wave sleep. Nat. Commun. *11*, 3240. https://doi.org/10.1038/s41467-020-17062-2.
53. Jursky, F., and Nelson, N. (1999). Developmental expression of the neurotransmitter transporter GAT3. J. Neurosci. Res. *55*, 394–399. https://doi.org/10.1002/(SICI)1097-4547(19990201)55:3<394::AID-JNR14>3.0.CO;2-E.
54. Bindu, D.S., Savage, J.T., Brose, N., Bradley, L., Dimond, K., Tan, C.X., and Eroglu, C. (2024). GEARBOCS: An Adeno Associated Virus Tool for In Vivo Gene Editing in Astrocytes. Preprint at bioRxiv, https://doi.org/10.1101/2023.01.17.524433 https://doi.org/10.1101/2023.01.17.524433.
55. van Hateren, J.H., and Ruderman, D.L. (1998). Independent component analysis of natural image sequences yields spatio-temporal filters similar to simple cells in primary visual cortex. Proc. R. Soc. Lond. B Biol. Sci. *265*, 2315–2320. https://doi.org/10.1098/rspb.1998.0577.
56. Pachitariu, M., Stringer, C., Dipoppa, M., Schröder, S., Rossi, L.F., Dalgleish, H., Carandini, M., and Harris, K.D. (2017). Suite2p: beyond 10,000 neurons with standard two-photon microscopy. Preprint at bioRxiv, https://doi.org/10.1101/061507 https://doi.org/10.1101/061507.
57. Mathis, A., Mamidanna, P., Cury, K.M., Abe, T., Murthy, V.N., Mathis, M.W., and Bethge, M. (2018). DeepLabCut: markerless pose estimation of user-defined body parts with deep learning. Nat. Neurosci. *21*, 1281–1289. https://doi.org/10.1038/s41593-018-0209-y.
58. Nath, T., Mathis, A., Chen, A.C., Patel, A., Bethge, M., and Mathis, M.W. (2019). Using DeepLabCut for 3D markerless pose estimation across species and behaviors. Nat. Protoc. *14*, 2152–2176. https://doi.org/10.1038/s41596-019-0176-0.
59. Aarts, E., Verhage, M., Veenvliet, J.V., Dolan, C.V., and van der Sluis, S. (2014). A solution to dependency: using multilevel analysis to accommodate nested data. Nat. Neurosci. *17*, 491–496. https://doi.org/10.1038/nn.3648.
60. Statsmodels: Econometric and Statistical Modeling with Python - SciPy Proceedings (2010). https://proceedings.scipy.org/articles/Majora-92bf1922-011.

Figures

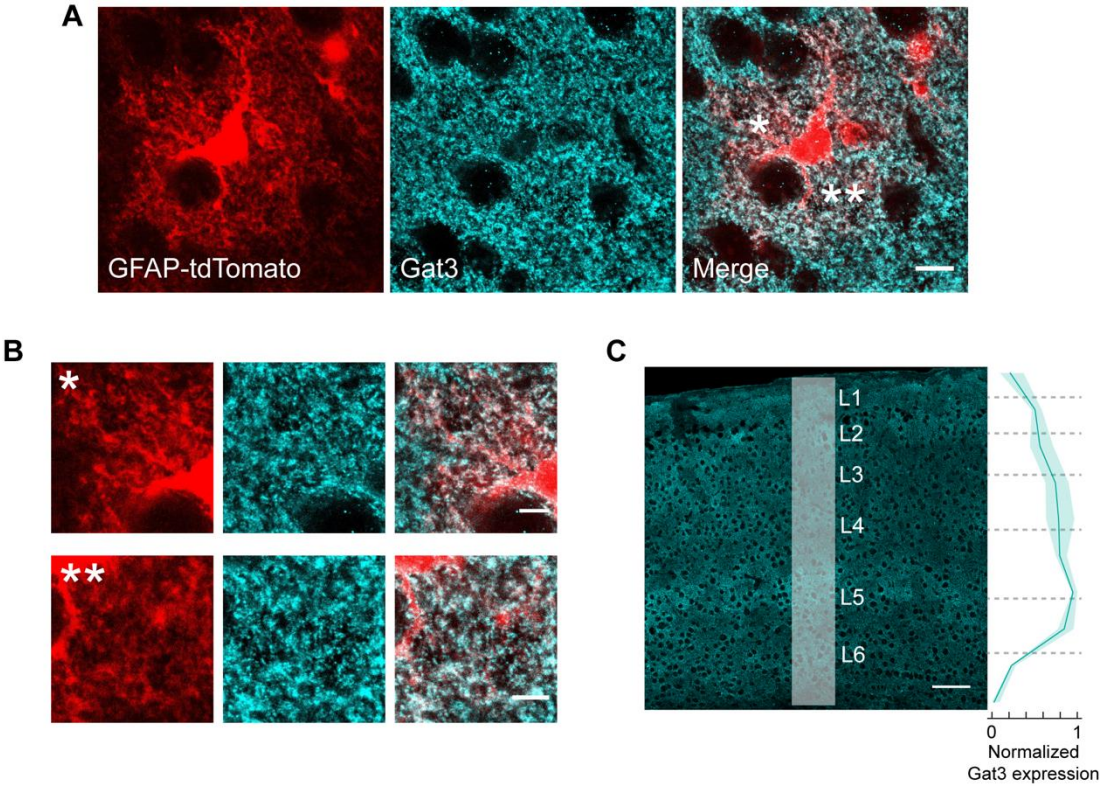

Figure 1. Characterization of Gat3 expression across cortical layers (A) High magnification (63x) merged image of GFAP promoter-driven tdTom+ astrocytes (red) and Gat3 (cyan). Co-localization is represented by white pixels (scale bar = 10 μm). White asterisks indicate parts of astrocytic processes with high Gat3 expression. (B) Magnification of Gat3 staining in parts labeled with the white asterisks in A (scale bar = 5 μm). (C) Quantification of Gat3 expression across cortical layers; expression density in white strip is shown at right (scale bar = 100 μm, n = 3 mice, shaded area = SEM).

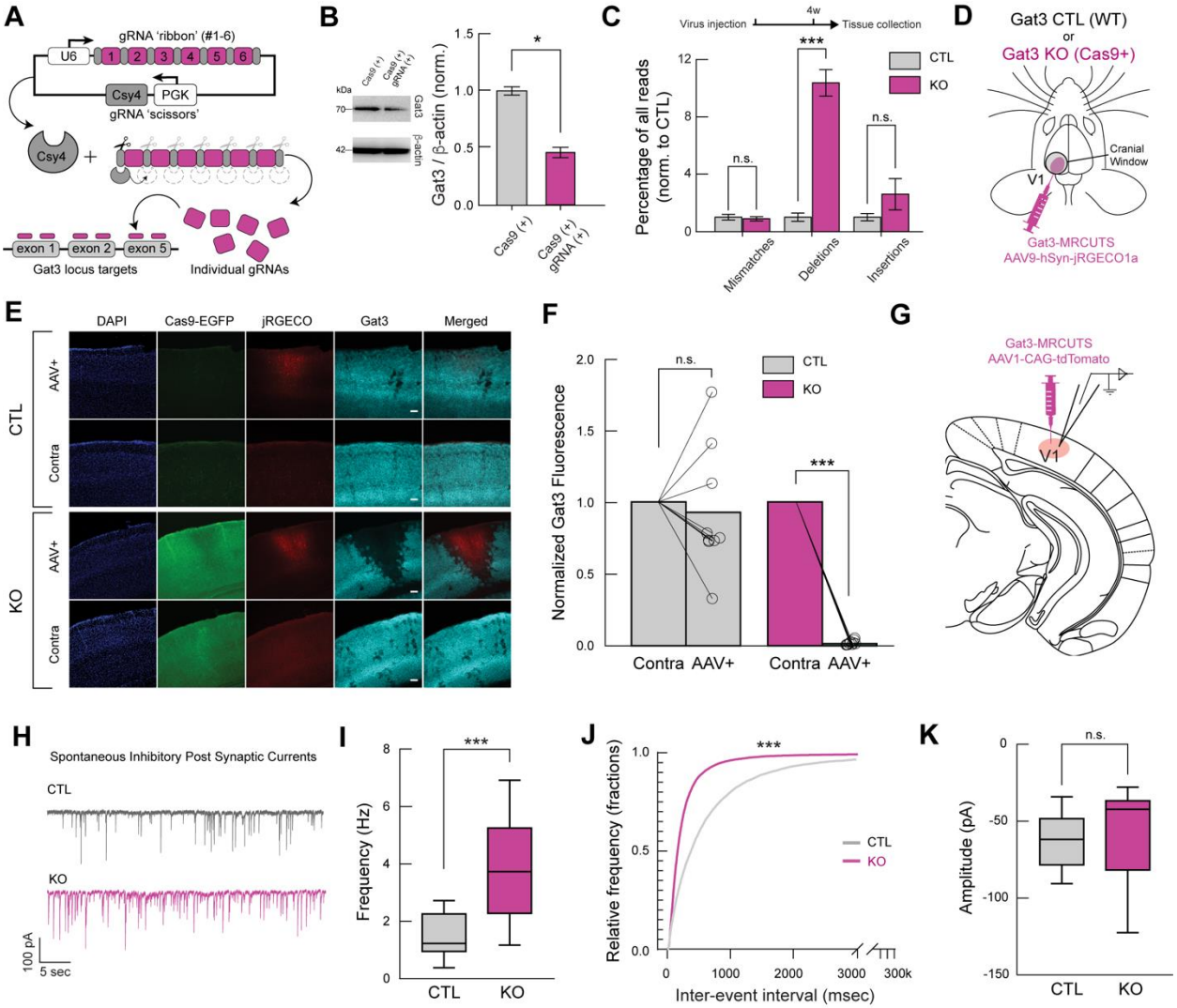

Figure 2. A Gat3-specific multiplexed CRISPR construct successfully knocks out Gat3 (A) Schematic diagram illustrating the construct design, which consists of six CRISPR KO sgRNAs targeting the mouse Gat3 gene. These sgRNAs are separated by Csy4 enzyme cleavage sites, allowing their individual release in virus-injected cells. (B) Western blot and its quantification showing efficient knockout of Gat3 in cultured astrocytes co-transfected with Cas9 and Gat3-MRCUTS plasmids compared to astrocytes transfected with Cas9 plasmid alone (n = 3 independent experiments, *, $p < 0.05$, two-tailed unpaired t-test, error bars = SEM). (C) DNA sequencing reads of one gRNA targeted region from mouse brain tissue collected after virus injection shows frequency of deletions at the target site in KO tissue (n.s., $p_{mismatches} = 0.723$; ***, $p_{deletions} < 0.001$; n.s., $p_{insertions} = 0.158$, two-tailed unpaired t-test, error bars = SEM). (D) Schematic of viral injections and cranial window implant over V1 for two-photon imaging. Viral constructs of the multiplexed gRNAs and red-shifted calcium indicator were co-injected in the left hemisphere of either wild-type mice or Cas9-expressing transgenic mice. (E) Representative immunohistochemistry images from a control and KO animal (scale bar = 100 μm, applies to all images in a row). (F) Comparison of Gat3 fluorescence intensity at the imaging sites and at the non-injected site within individual slices. Baseline intensity was determined by the non-injected right (contralateral) hemisphere to account for variability between slices ($n_{control}$ = 9 slices, 4 mice, n.s., $p_{control} = 0.443$; $n_{Gat3\ KO}$ = 10 slices, 4 mice, ***, $p_{Gat3\ KO} < 0.001$, Mann-Whitney U test). (G) Schematic of *ex vivo* whole-cell patch clamp electrophysiology set-up. Gat3-MRCUTS was co-injected with a tdTomato virus to label the injection site for recordings. (H) Representative traces of sIPSCs of L2/3 pyramidal neurons in visual cortex brain slices. (I) Comparison of

frequency of sIPSCs between control and Gat3 KO brain slices ($n_{control}$ = 20 cells, $n_{Gat3\ KO}$ = 23 cells, ***, $p < 0.001$, two-tailed unpaired t-test). (J) Cumulative probability histograms for inter-event intervals (***, $p < 0.001$, Kolmogorov-Smirnov test). (K) Comparison of average amplitude of sIPSCs (n.s., $p = 0.9351$, two-tailed unpaired t-test).

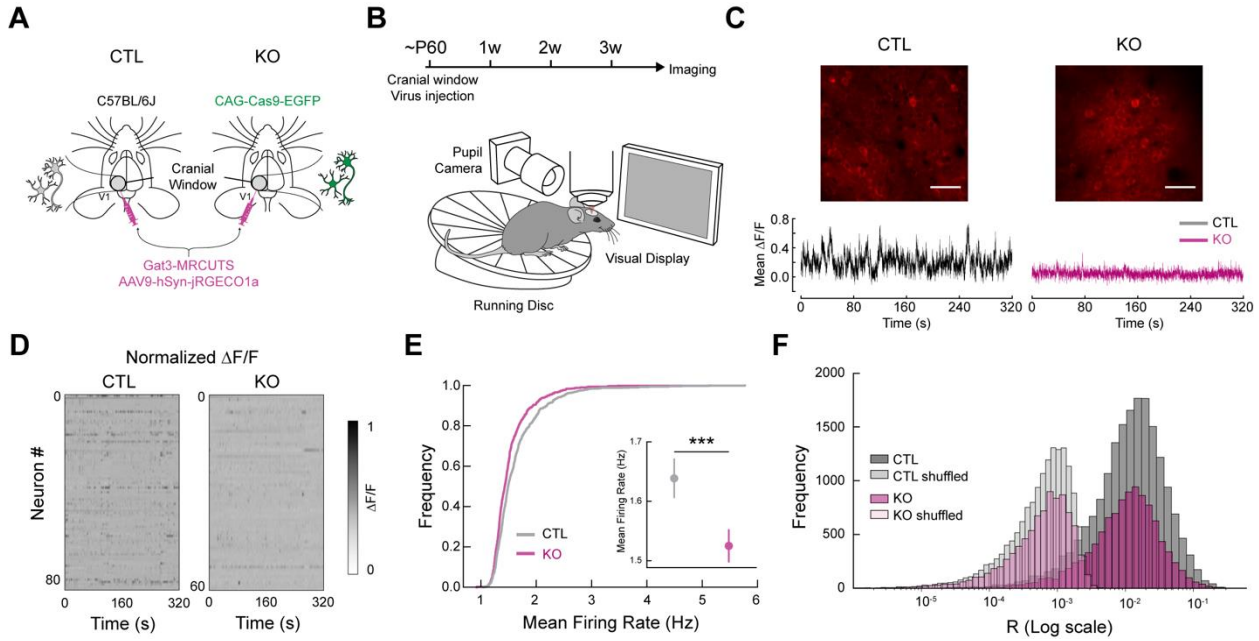

Figure 3. Genetic knockout of Gat3 in the visual cortex alters spontaneous activity of single neurons (A) Schematic of control and experimental mice preparation. Both control mice (wild-type) and experimental mice (transgenic mice with cells constitutively expressing Cas9-EGFP under CAG promoter) received co-injection of Gat3-MRCUTS and a neuronal calcium sensor (jRGECO1a) in V1 during stereotactic surgeries. (B) Two-photon imaging set-up consisting of a running wheel and a pupil camera to acquire locomotion and pupil dynamics, respectively. (C) Top: Example field-of-view (FOV) images of an imaging session from each group (scale bar = 50 μm). Bottom: Example average Ca^{2+} traces from a control and a Gat3 KO mouse. The normalized Ca^{2+} traces of all neurons within the same FOV were averaged. (D) Representative heatmaps of normalized spontaneous calcium activity of neurons in each session from each group. (E) Firing rates of individual neurons in control and Gat3 KO group. Inset shows the average firing rates of all neurons from each group ($n_{control}$ = 838 neurons, 4 mice, $n_{Gat3\ KO}$ = 606 neurons, 4 mice, ***, $p < 0.001$, Linear mixed effects model (LME) t-stats, see Methods, error bars = SEM). (F) Distribution of pairwise correlation coefficients of neurons ($n_{control}$ = 31460 pairs, $n_{Gat3\ KO}$ = 18004 pairs, n.s., $p = 0.224$, LME t-stats).

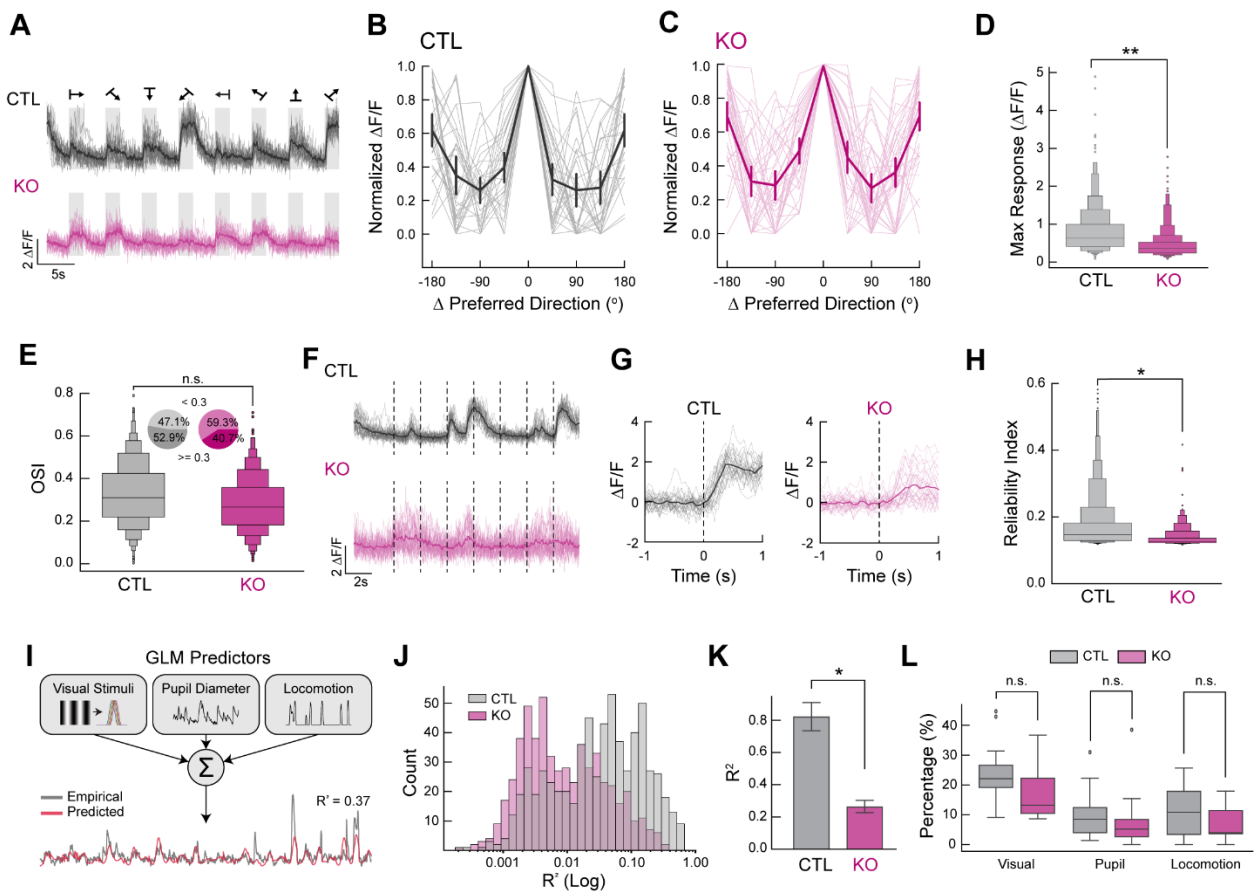

Figure 4. Genetic knockout of Gat3 in the visual cortex alters the visual response properties of neurons (A) Example Ca^{2+} traces of a single neuron from control (top) and Gat3 KO (bottom) during presentation of drifting gratings. The average of all trials is plotted in a dark line overlaid on the lighter individual trial traces (16 trials in total). (B) Representative tuning curves of control individual neurons (in lighter shade) and the average tuning curve (in bold) of all neurons in each FOV centered around their preferred orientation ($n_{control}$ = 32 neurons, error bars = SEM). (C) Same as B but for Gat3 KO ($n_{Gat3\ KO}$ = 38 neurons, error bars = SEM). (D) Average maximum response magnitudes of neurons to their preferred grating orientation. Visually responsive neurons were pooled across animals within each group ($n_{control}$ = 526 neurons, 4 mice, $n_{Gat3\ KO}$ = 366 neurons, 4 mice, **, $p < 0.01$, LME t-stats). (E) Comparison of OSI distribution of visually responsive neurons between the two groups (n.s., $p = 0.183$, LME t-stats). Insets show the percentage of cells with OSI greater or less than 0.3. (F) Example Ca^{2+} traces of a single neuron from control (top) and Gat3 KO (bottom) during natural movies where the dotted lines indicate the onset of a movie. The average of all trials is plotted in a dark line overlaid on the lighter individual trial traces (32 trials in total). (G) Example plots showing variability of each trial response (in lighter shade) of a single neuron to a natural movie. 0 s indicates the stimulus onset. (H) Reliability indices of neurons to their preferred stimuli in control and Gat3 KO group ($n_{control}$= 707 neurons, 4 mice, $n_{Gat3\ KO}$ = 436 neurons, 4 mice, *, $p < 0.05$, LME t-stats). (I) Generalized Linear Model (GLM)-based single neuron encoding model of visual stimulus information, pupil dynamics, and running speed. Variance explained (R^2) is computed to assess the encoding property of neurons. (J) Distribution of R^2 of individuals neurons from each group ($n_{control}$ = 647 neurons, 4 mice, $n_{Gat3\ KO}$ = 565 neurons, 4 mice). (K) Comparison of average R^2 values of individual neurons between the two groups (*, $p < 0.05$, LME t-stats, error bars = SEM). (L) Proportions of neurons encoding each parameter (visual stimuli, pupil dynamics, and movement) from each imaged population (n.s., $p_{Visual\ stimuli}$ = 0.116; n.s., p_{Pupil} = 0.662; n.s., $p_{Movement}$ = 0.172, LME t-stats).

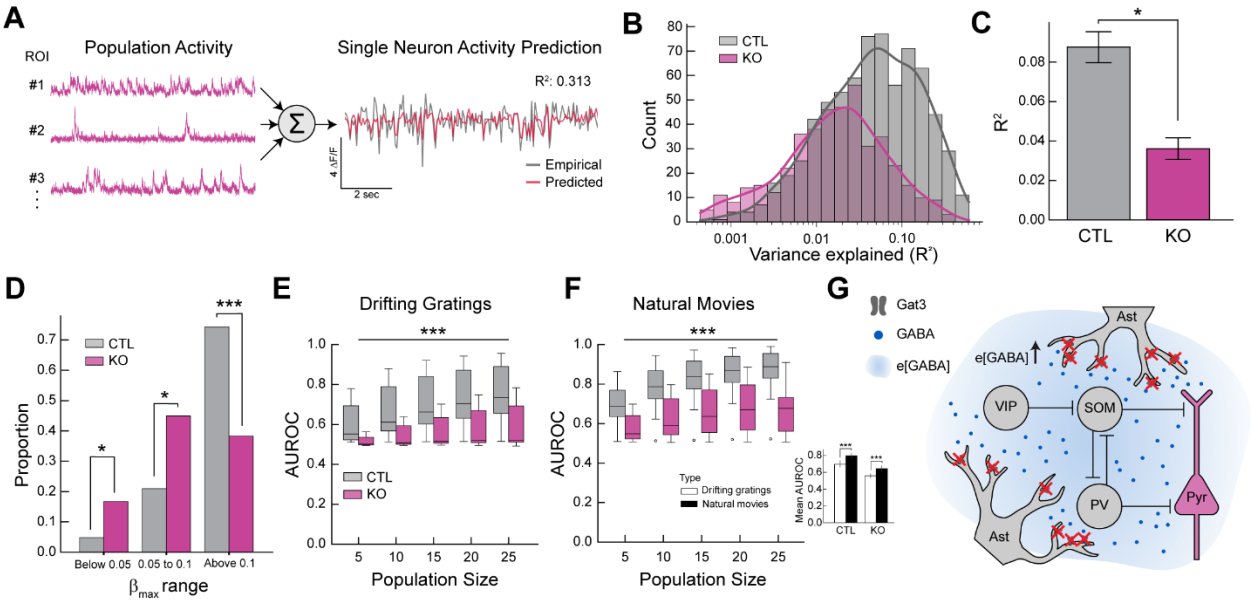

Figure 5. Genetic knockout of Gat3 alters population-level properties of cortical neurons (A) Schematic of a single neuron encoding model of population activity using GLM. Calcium traces of randomly sampled neurons in a fixed population size were used to train a GLM model for prediction of the target neuron's activity. (B) Distribution of R^2 values of individual neurons ($n_{control}$= 707 neurons, 4 mice, $n_{Gat3\ KO}$ = 436 neurons, 4 mice, training population size = 20 neurons). (C) Comparison of average R^2 value of all neurons between two groups (*, $p < 0.05$, LME t-stats, error bars = SEM). (D) The maximum value of the predictor weights (β) from each neuron's GLM fitting was extracted and grouped into ranges of below 0.05, 0.05 to 0.1, and above 0.1. The difference in proportions of the weights showed the different level of encoding of other neurons between the two groups (*, $p < 0.05$, ***, $p < 0.001$, Mann-Whitney U test). (E) SVM-based decoding analysis of neuronal population activity induced by drifting gratings in neuronal populations of various sizes. Comparison of decoding accuracy of visual stimulus information (Area Under the Receiver Operating Characteristic curve) of populations between two groups ($n_{control}$ = 12 sessions, 4 mice, $n_{Gat3\ KO}$ = 9 sessions, 4 mice, ***, $p < 0.001$, 2-way ANOVA). (F) Same as E but for natural movies ($n_{control}$ = 11 sessions, 4 mice, $n_{Gat3\ KO}$ = 11 sessions, 4 mice, ***, $p < 0.001$, 2-way ANOVA). Inset: comparison of average AUROC between different visual stimuli within each group (***, $p < 0.001$, Mann-Whitney U test, error bars = SEM). (G) A simplified diagram of a visual cortex L2/3 microcircuit consisting of neurons and astrocytes. The microcircuit contains different types of inhibitory neurons that exert inhibitory or disinhibitory effects on pyramidal neurons. Extra-synaptic expression of Gat3 in astrocytic processes allows astrocytes to control extracellular GABA levels that may differentially influence a wide network of cells.

Supplementary Figures

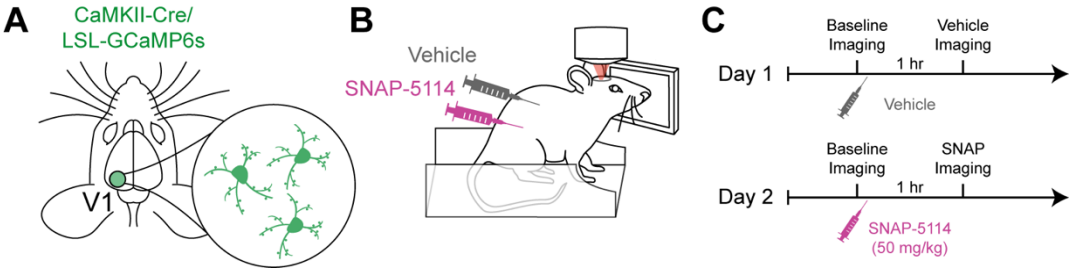

Figure S1. Experimental design and timeline (A) Transgenic mice expressing Cre-dependent GCaMP6s in excitatory neurons (CaMKII-Cre) had cranial windows implanted over V1 and were imaged 1-2 weeks later. (B) Neuronal responses to visual stimuli were imaged using two-photon microscopy in head-fixed mice. Following baseline imaging, either vehicle (5% DMSO in corn oil) or SNAP-5114 (50mg/kg) was injected i.p. followed by imaging the same field-of-view (FOV). (C) Timeline for imaging. Imaging after vehicle and SNAP-5114 treatment was performed on the same FOV on two different days. Both were compared to baseline imaging.

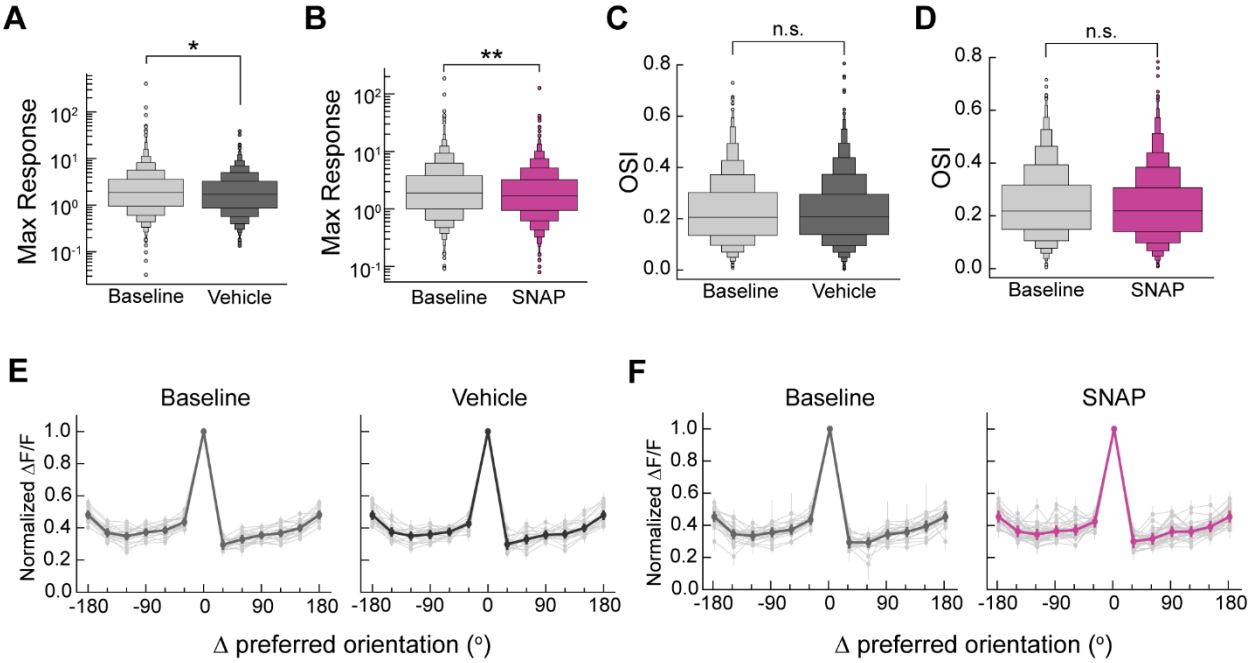

Figure S2. Systemic administration of SNAP-5114 affects select V1 neuronal response properties (A) Average maximum response magnitude of visually responsive neurons before and after vehicle administration. ($n_{baseline}$ = 1798 neurons, $n_{vehicle}$ = 1648 neurons, $n_{baseline}$ = 20 sessions, $n_{vehicle}$ = 20 sessions, *, $p < 0.05$, LME t-stats). (B) Same as A but before and after SNAP-5114 administration ($n_{baseline}$ = 1709 neurons, $n_{SNAP\text{-}5114}$ = 2002 neurons, $n_{baseline}$ = 25 sessions, $n_{SNAP\text{-}5114}$ = 38 sessions, **, $p < 0.01$, LME t-stats). (C) Orientation selectivity index (OSI) distribution of all visually responsive neurons before and after vehicle administration ($n_{baseline}$ = 1798 neurons, $n_{vehicle}$ = 1648 neurons, $n_{baseline}$ = 20 sessions, $n_{vehicle}$ = 20 sessions, n.s., $p = 0.359$, LME t-stats). (D) Same as C but before and after SNAP-5114 treatment ($n_{baseline}$ = 1709 neurons, $n_{SNAP\text{-}5114}$ = 2002 neurons, $n_{baseline}$ = 25 sessions, $n_{SNAP\text{-}5114}$ = 38 sessions, n.s., $p = 0.622$, LME t-stats). (E) Average tuning curves of visually responsive neurons per session (in lighter shade) before and after vehicle administration. Average tuning curve of all sessions is in bold ($n_{baseline}$ = 1798 neurons, $n_{vehicle}$ = 1648 neurons, $n_{baseline}$ = 20 sessions, $n_{vehicle}$ = 20 sessions, error bars = SEM). (F) Same as E but before and after SNAP-5114 treatment ($n_{baseline}$ = 1709 neurons, $n_{SNAP\text{-}5114}$ = 2002 neurons, $n_{baseline}$ = 25 sessions, $n_{SNAP\text{-}5114}$ = 38 sessions, error bars = SEM). All sessions were from 5 mice studied under vehicle and SNAP-5114 treatment conditions (see Figure S1).

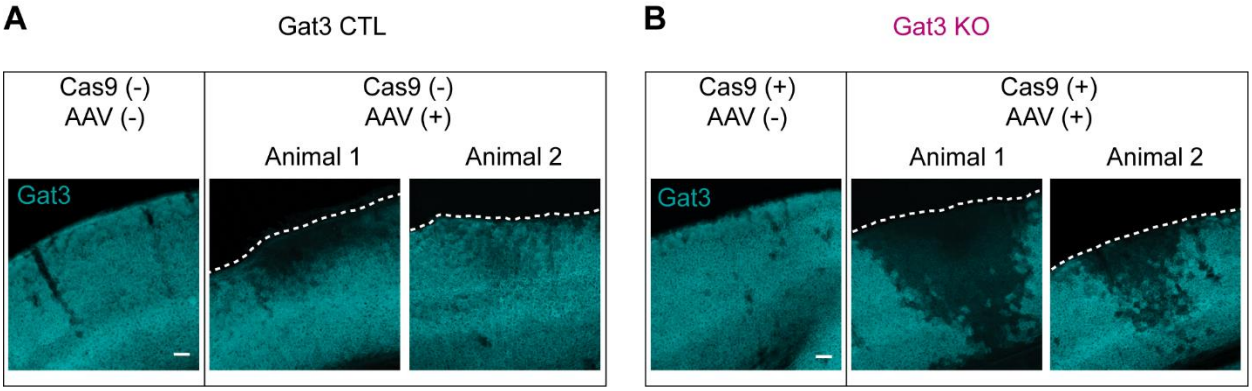

Figure S3. Gat3 expression changes in control and KO brain slices (A) Coronal slices of control animal brains. Left column: hemisphere with no virus injection. Right columns: hemispheres with virus injection from two different animals. Reduced superficial Gat3 expression is observed in control animals with variability between animals. Animal 1 represents the maximal effect of AAV injection on Gat3 expression and animal 2 represents a more typical effect (scale bar = 100 μm, applies to all images). (B) Same as A but for Gat3 KO animal brains. Compared to the injected hemispheres of control animals, the injected hemispheres of Gat3 KO animals showed a more severe reduction of Gat3 expression throughout the cortical layers (scale bar = 100 μm, applies to all images). White dotted lines indicate pial surface of the cortex.

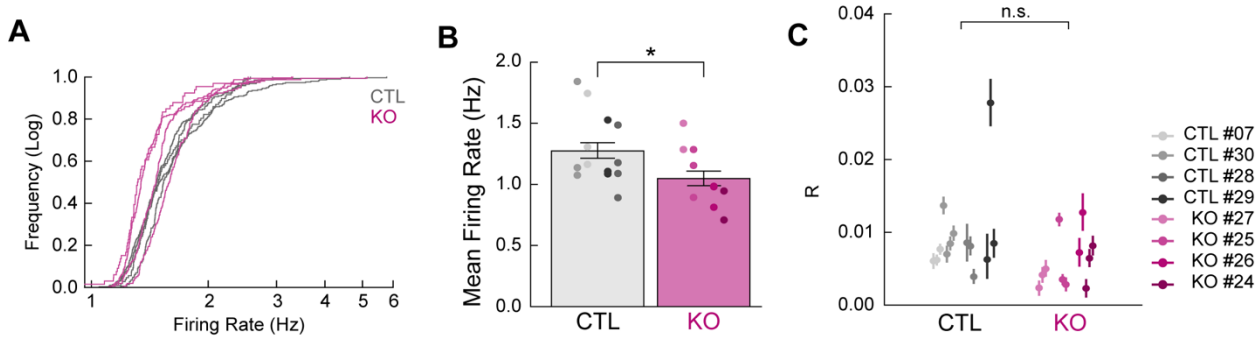

Figure S4. Comparisons of average firing rates of single neurons and neuron-to-neuron pairwise correlation during spontaneous activity (A) Empirical cumulative distribution functions plot of firing rates for each animal shown as individual traces ($n_{control}$ = 4 mice, $n_{Gat3\ KO}$ = 4 mice). (B) Average firing rates of neurons; different sessions per animal indicated by different colors ($n_{control}$ = 13 sessions, 4 mice, $n_{Gat3\ KO}$ = 11 sessions, 4 mice, *, $p < 0.05$, LME t-stats, error bars = SEM). (C) Average neuron-to-neuron pairwise correlation coefficient of neurons per session by animal ($n_{control}$ = 13 sessions, 4 mice, $n_{Gat3\ KO}$ = 11 sessions, 4 mice, n.s., $p = 0.224$, LME t-stats, error bars = SEM).

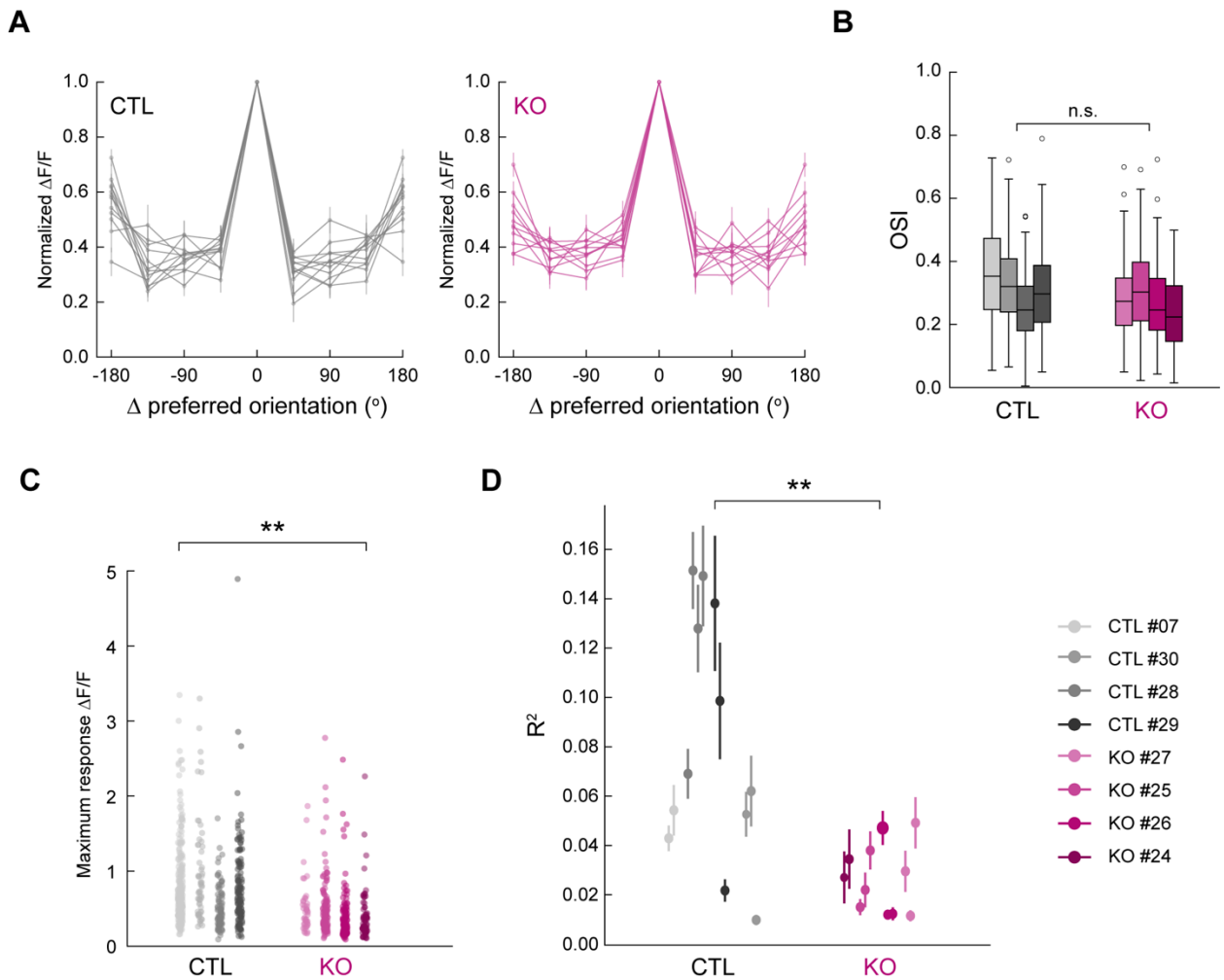

Figure S5. Comparisons of visual responses of single neurons to drifting gratings (A) Average tuning curves of neurons by session in each group ($n_{control}$ = 12 sessions, 4 mice, $n_{Gat3\ KO}$ = 11 sessions, 4 mice, error bars = SEM). (B) OSI distribution of neurons for each animal ($n_{control}$ = 4 mice, $n_{Gat3\ KO}$ = 4 mice, n.s., p = 0.183, LME t-stats, error bars = SEM). (C) Maximum response magnitudes of visually responsive neurons to their preferred gratings compared by animal ($n_{control}$ = 4 mice, $n_{Gat3\ KO}$ = 4 mice, **, $p < 0.01$, LME t-stats). (D) Average R^2 of neurons for single neuron encoding of drifting gratings and behavioral variables by sessions ($n_{control}$ = 12 sessions, 4 mice, $n_{Gat3\ KO}$ = 11 sessions, 4 mice, **, $p < 0.01$, LME t-stats, error bars = SEM).

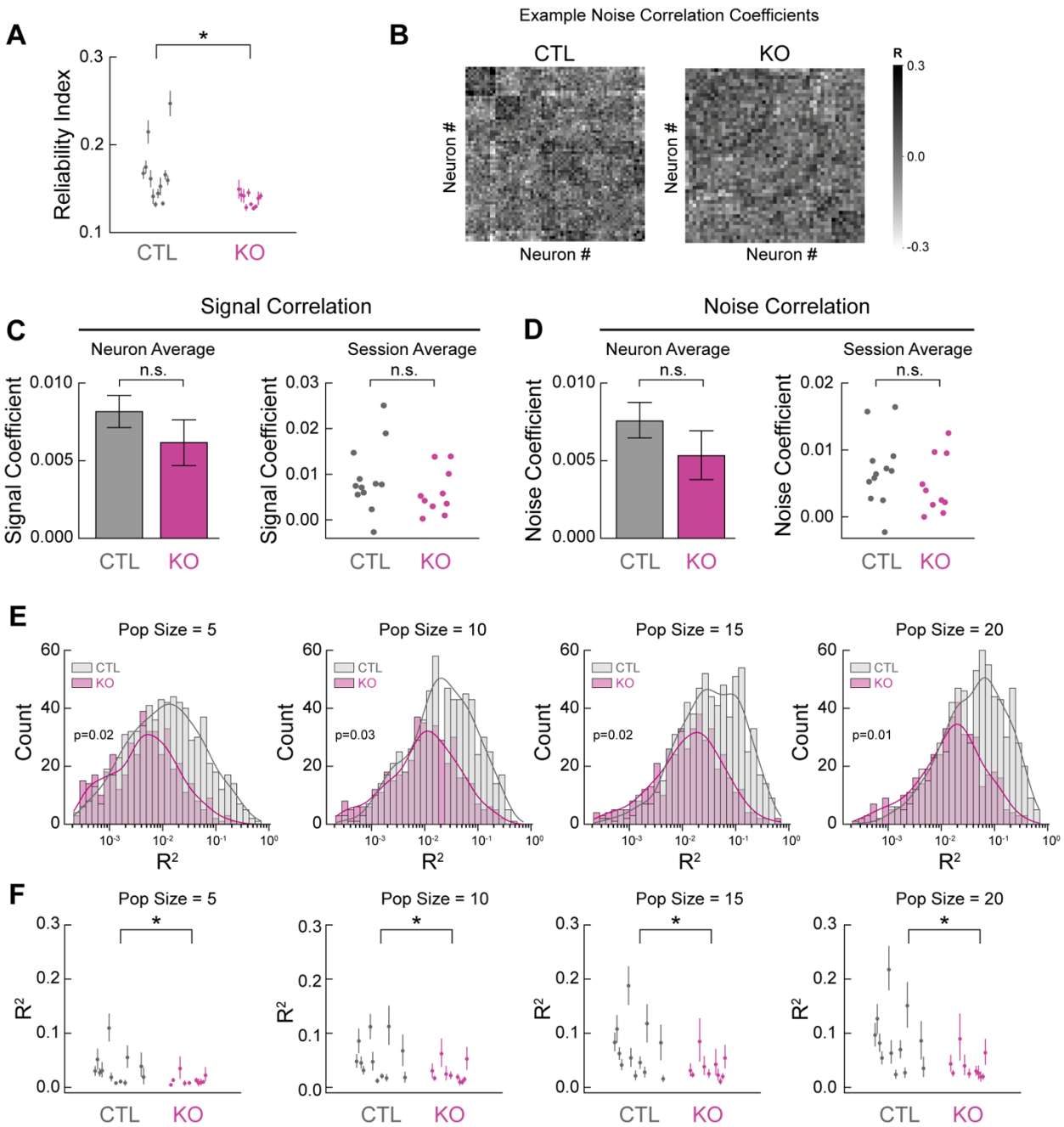

Figure S6. Comparisons of neuronal responses to natural movies (A) Average reliability indices of neurons per session ($n_{control}$ = 12 sessions, 4 mice, $n_{Gat3\ KO}$ = 10 sessions, 4 mice, *, $p < 0.05$, LME t-stats, error bars = SEM). (B) Representative noise correlation coefficient matrices. (C) Average signal correlation coefficients between pairs of neurons ($n_{control}$ = 24929 pairs, $n_{Gat3\ KO}$ = 10110 pairs, $n_{control}$ = 12 sessions, 4 mice, $n_{Gat3\ KO}$ = 10 sessions, 4 mice, n.s., $p = 0.741$, LME t-stats, error bars = SEM). (D) Average noise correlation coefficients between pairs of neurons ($n_{control}$ = 24929 pairs, $n_{Gat3\ KO}$ = 10110 pairs, $n_{control}$ = 12 sessions, 4 mice, $n_{Gat3\ KO}$ = 10 sessions, 4 mice, n.s., $p = 0.1349$, LME t-stats, error bars = SEM). (E) R^2 distribution of population activity encoding GLM model performance as a function of different population sizes of neurons used for model training. (F) Average R^2 values per session and per animal for each population size ($n_{control}$ = 12 sessions, 4 mice, $n_{Gat3\ KO}$ = 10 sessions, 4 mice, *, $p_{5\text{-}20} < 0.05$ each, LME t-stats, error bars = SEM).